Article

Systemic and intrinsic functions of ATRX in glial cell fate and CNS myelination in male mice

Megan E. Rowland[1,2], Yan Jiang[2,3], Sarfraz Shafiq[2,4], Alireza Ghahramani[2,4], Miguel A. Pena-Ortiz[2,5], Vanessa Dumeaux[4,6] & Nathalie G. Bérubé[2,3,4,5,6] ✉

Myelin, an extension of the oligodendrocyte plasma membrane, wraps around axons to facilitate nerve conduction. Myelination is compromised in ATR-X intellectual disability syndrome patients, but the causes are unknown. We show that loss of *ATRX* leads to myelination deficits in male mice that are partially rectified upon systemic thyroxine administration. Targeted ATRX inactivation in either neurons or oligodendrocyte progenitor cells (OPCs) reveals OPC-intrinsic effects on myelination. OPCs lacking ATRX fail to differentiate along the oligodendrocyte lineage and acquire a more plastic state that favors astrocytic differentiation in vitro and in vivo. ATRX chromatin occupancy in OPCs greatly overlaps with that of the chromatin remodelers CHD7 and CHD8 as well as H3K27Ac, a mark of active enhancers. Overall, our data indicate that ATRX regulates the onset of myelination systemically via thyroxine, and by promoting OPC differentiation and suppressing astro-gliogenesis. These functions of ATRX identified in mice could explain white matter pathogenesis observed in ATR-X syndrome patients.

Myelin is an extension of the oligodendrocyte (OL) plasma membrane that wraps itself around axons to increase conduction velocity, enabling efficient propagation of action potentials. A series of events are necessary to produce myelin, including proliferation and migration of oligodendrocyte precursor cells (OPCs), recognition of recipient axons, membrane expansion, wrapping of axons and the appropriate production of membrane components and myelin proteins for compaction[1].

In the developing neocortex, the generation of neurons from neural progenitor cells eventually shifts towards production of astrocytes and then OLs[2]. The majority of primitive OPCs are generated postnatally from neural stem cells (NSCs) and intermediate glial progenitor cells (iGCs) through the expression of the oligodendrocyte basic-helix-loop-helix transcription factors Olig1 and Olig2[3]. Olig2 is expressed in gliogenic progenitors where it acts as a repressor of neuronal differentiation. Postnatally, Olig2 has been reported to support OL differentiation from OPCs and to suppress astrocytic lineage in these cells[4–7]. Downstream of Olig2, the SRY-box transcription factor 10 (Sox10) participates in a positive feedback loop to establish the OPC lineage[8–10]. Notably, Sox10 activates several OPC-critical genes, including *Chondroitin sulfate proteoglycan* (*Cspg4*; protein: neural glial antigen 2 (NG2)) and *Platelet-derived growth factor receptor α* (*Pdgfrα*)[11–13]. NG2 is a surface type I transmembrane core protein involved in cell migration and proliferation[14], whereas PDGFRα promotes OPC proliferation, migration and survival[15,16]. Further commitment to the OL lineage starts with the generation of immature oligodendrocytes (iOLs) which, after cell cycle exit, express myelin regulatory factor (MRF)[17]. As iOLs mature and contact axons, they

[1]Department of Biochemistry, Schulich School of Medicine and Dentistry, Western University, London, ON, Canada. [2]Children's Health Research Institute, Division of Genetics & Development, London, ON, Canada. [3]Department of Paediatrics, Schulich School of Medicine and Dentistry, Western University, London, ON, Canada. [4]Department of Anatomy and Cell Biology, Schulich School of Medicine and Dentistry, Western University, London, ON, Canada. [5]Graduate Program in Neuroscience, Western University, London, ON, Canada. [6]Department of Oncology, Schulich School of Medicine and Dentistry, Western University, London, ON, Canada. ✉e-mail: nberube@uwo.ca

become highly branched and upregulate several myelin sheath proteins in order to encompass the axon[1,18]. The expression of myelin proteins is complex and regulated by several different transcription factors including the aforementioned Olig1[19], Sox10 [19,20] and MRF[17] but also Sp1[21], Nkx2.2[22] and the ligand-bound thyroid hormone receptor[23–25].

Myelination has been studied extensively in the context of demyelinating diseases like multiple sclerosis and leukodystrophies[26]. However, myelin deficits are also frequently observed in neurodevelopmental cognitive disorders like autism and schizophrenia and can contribute to intellectual disability[27–29]. This is exemplified by the ATR-X syndrome, an intellectual disability disorder caused by abnormalities in the ATRX chromatin remodeling protein[30]. Affected males often exhibit cognitive dysfunction, seizures and autistic features, among other developmental defects[31–35]. ATR-X syndrome patients also display abnormal myelination with a prevalence of 44%[33,34] making white matter abnormalities a supporting feature of the diagnosis.

ATRX belongs to the Switch/Sucrose non-fermenting (Swi/Snf) family of chromatin remodelers[36], and can regulate gene expression through several mechanisms. In the newborn cortex, ATRX represses expression of imprinted genes by fostering long-range chromatin interactions mediated by CCCTC-binding factor (CTCF) and cohesin[37,38]. In embryonic stem cells, it promotes maintenance of the repressive H3K27me3 histone mark at polycomb target genes[39]. On the other hand, ATRX can promote gene transcription through the incorporation of histone H3.3 and facilitating RNA PolII elongation through G-rich sequences[40,41]. In testes, ATRX regulates imprinted genes[42] associates with the androgen receptor and facilitates transcription of its target genes[43]. ATRX also promotes the expression of α-globin by negatively regulating the histone variant macroH2A[44].

The molecular and cellular basis of white matter abnormalities associated with ATRX dysfunction has not yet been investigated. Here, we report that deletion of *Atrx* in the central nervous system causes hypomyelination. While myelin levels and OL numbers were partially recovered upon administration of the thyroid hormone thyroxine (T4), this treatment failed to replenish OPCs, indicating that ATRX is required to maintain these progenitors independently of circulating T4 levels. Indeed, targeted inactivation of *Atrx* in Sox10-expressing OPCs resulted in hypomyelination, revealing cell autonomous functions of ATRX in OPCs. We show that ATRX occupies and maintains *Olig2* gene expression. In the absence of ATRX, OPCs tend to revert to a more malleable state, and gain the ability to differentiate into astrocyte-like cells. We conclude that ATRX deficiency affects the developmental trajectory of glial precursors, which could be the underlying cause of defective myelination in the associated ATR-X syndrome.

Results

Decreased myelination in the Atrx[FoxG1Cre] mouse forebrain

We previously reported that postnatal health and longevity are adversely affected in mice with ATRX deficiency in the forebrain, anterior pituitary and liver (*Atrx*[FoxG1cre] mice)[45,46]. These mice have a reduced lifespan, growth and hormone abnormalities, including low circulating levels of IGF-1 and T4[45,46] and exhibit aberrant gene expression in the liver[45]. To identify potential forebrain related differences in transcription between control and *Atrx*[FoxG1Cre] mice, we performed a microarray analysis of 3 littermate-matched pairs of P17 control and *Atrx*[FoxG1Cre] mice. Microarray analysis revealed a significant downregulation of genes involved in myelination and oligodendrocyte morphology (Fig. 1a, b, $p < 0.05$). Moreover, downregulated genes are highly expressed in mouse oligodendrocytes according to the Allan Brain Atlas single cell RNA gene sets (Fig. 1c). Given previous reports of white matter abnormalities in ATR-X syndrome patients[33,34], we further explored whether the mice exhibit a similar phenotype. We examined the level of well-established myelin markers by immunofluorescence staining of brain cryosections. The results showed decreased level of myelin oligodendrocyte glycoprotein (MOG) and myelin basic protein (MBP) in the corpus callosum and adjacent cortex in *Atrx*[FoxG1Cre] compared to control mice at P20 (Fig. 1d). Western blot analysis of myelin associated glycoprotein (MAG), MOG and MBP showed that myelin protein expression is significantly decreased in *Atrx*[FoxG1Cre] forebrain compared to littermate matched controls ($n = 4$ each genotype; Student's *T*-test, MAG $p = 0.006$, MOG $p = 0.005$, MBP $p = 0.009$) (Fig. 1e, f). These data strongly suggest that the *Atrx*[FoxG1Cre] CNS is hypomyelinated.

Postnatal thyroxine treatment partially restores myelination deficits in Atrx[FoxG1Cre] mice

Circulating levels of the thyroid hormone T4 in *Atrx*[FoxG1Cre] mice are less than half that of controls, most likely stemming from the deletion of *Atrx* in the anterior pituitary in these mice[45,46]. The thyroid hormone receptor is a transcription factor that requires its ligand, triiodothyronine (T3), to promote OL differentiation and the expression of several myelin genes[47–52]. We therefore tested whether postnatal administration of the prohormone T4 might rescue hypomyelination in *Atrx*[FoxG1Cre] mice. We performed daily injections of 0.1 mg/kg L-thyroxine (T4) or PBS from P0 to P14, as outlined in Fig. 2a, a dose previously shown to successfully elevate circulating T4 to control levels in *Atrx*[FoxG1Cre] mice[45].

We first quantified the number of OLs after T4 treatment by immunofluorescence staining of P14 brain cryosections, using an antibody specific for the pan-OL marker Olig2. We observed a significant reduction of the proportion of Olig2+ cells (representing all OPCs and OLs) in the *Atrx*[FoxG1Cre] corpus callosum (27.6% of total DAPI+ cells) compared to controls (44.9% of total DAPI+ cells) and that this was partially recovered in *Atrx*[FoxG1Cre] mice treated with T4 (32.3%) ($n = 3$ for each genotype; $p = 0.0013$, one-way ANOVA) (Fig. 2b). We also counted the proportion of OPCs or OLs in the corpus callosum of control and *Atrx*[FoxG1Cre] brain cryosections at P14, marked by PDGFRα and adenomatous polyposis coli (APC), respectively. While the proportion of PDGFRα+ OPCs is lower in *Atrx*[FoxG1Cre] mice (12.8%) compared to controls (23.9%), it was not improved upon T4 treatment (11.7%) ($n = 3$ each genotype; $p = 0.0018$, one-way ANOVA) (Fig. 2c). The proportion of differentiated APC+ OLs was decreased in the *Atrx*[FoxG1Cre] corpus callosum (11%) compared to controls (29.2%) and was partially recovered (20.4%) following T4 treatment ($n = 3$ for each genotype; $p = 0.0018$ one-way ANOVA) (Fig. 2d), suggesting that thyroxine can only remediate differentiation defects.

To confirm that T4 administration promotes the differentiation of ATRX-null OPCs, we performed qRT-PCR for several established myelin genes including *Mag, Mog, Mbp* and *Plp1* (*Proteolipid protein 1*). The level of these RNA transcripts was elevated in T4- vs PBS-treated *Atrx*[FoxG1Cre] mice, but the extent of rescue did not reach control levels for *Mag* and *Mog* ($n = 3$–5 each genotype; *Mag* $p = 0.0008$; *Mog* $p = 0.0001$, *Mbp* $p = 0.17$, *Plp* $p = 0.001$ by one-way ANOVA) (Fig. 2e). Similarly, Western blot analysis of MAG, MOG and MBP showed some rescue of myelin protein levels in T4-treated *Atrx*[FoxG1Cre] forebrain extracts ($n = 3$ each genotype MAG $p = 0.026$; MOG $p = 0.027$, MBP $p = 0.035$ by one-way ANOVA) (Fig. 2f). Immunofluorescence staining of MOG and MBP in *Atrx*[FoxG1Cre] forebrain cryosections also showed improved myelination after T4 administration (Fig. 2g). Taken together, these results suggest that hypomyelination in *Atrx*[FoxG1Cre] mice is due to a reduced number of OPCs and OLs and that T4 treatment stimulates OPC differentiation without increasing OPC numbers, which could explain the incomplete effect of T4 treatment on the extent myelination.

Targeted ablation of Atrx in neurons does not affect myelination

The results of the T4 experiments suggested that ATRX is required in the central nervous system to support normal myelination, but it was
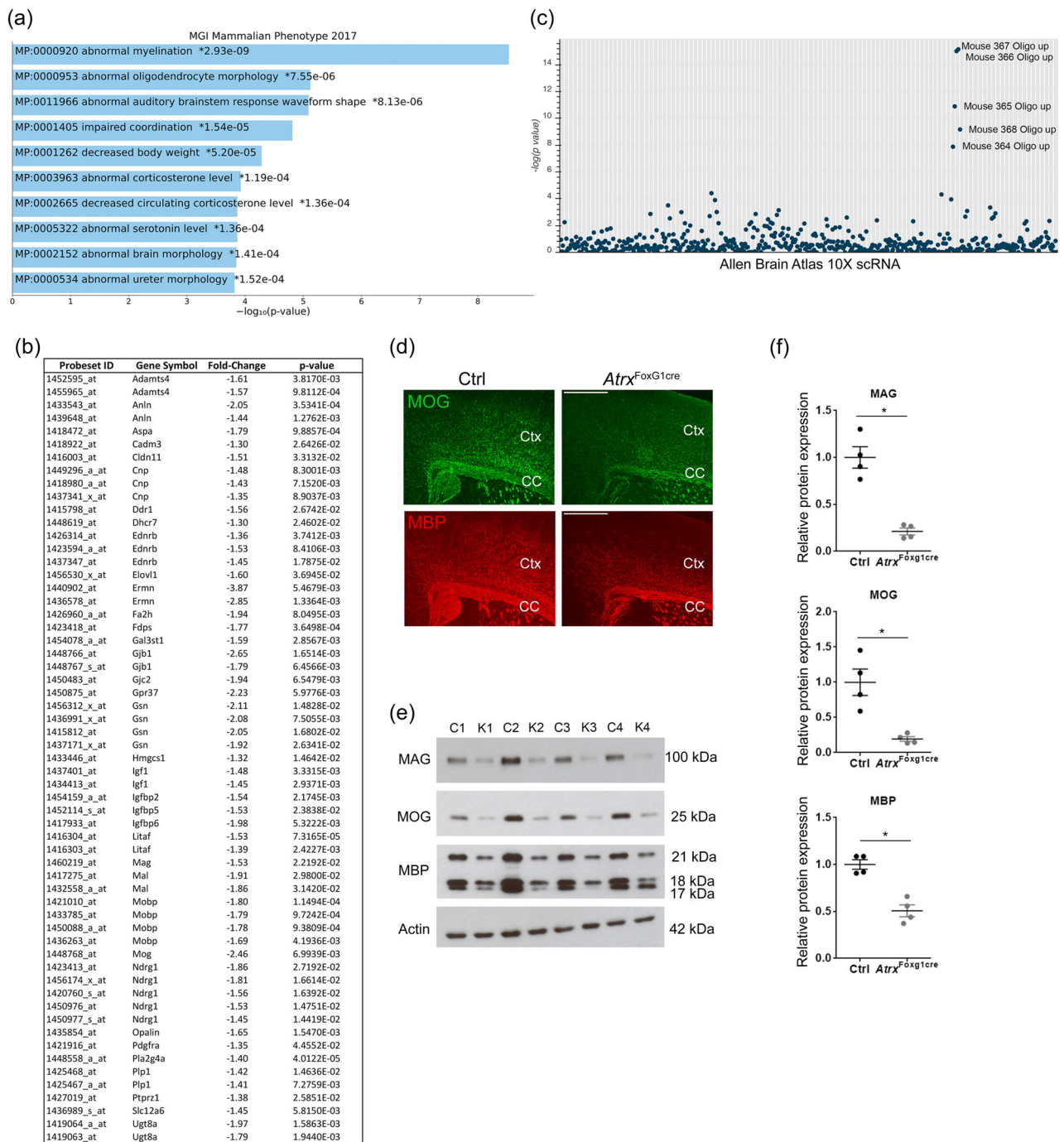
(a)

MGI Mammalian Phenotype 2017

- MP:0000920 abnormal myelination *2.93e-09
- MP:0000953 abnormal oligodendrocyte morphology *7.55e-06
- MP:0011966 abnormal auditory brainstem response waveform shape *8.13e-06
- MP:0001405 impaired coordination *1.54e-05
- MP:0001262 decreased body weight *5.20e-05
- MP:0003963 abnormal corticosterone level *1.19e-04
- MP:0002665 decreased circulating corticosterone level *1.36e-04
- MP:0005322 abnormal serotonin level *1.36e-04
- MP:0002152 abnormal brain morphology *1.41e-04
- MP:0000534 abnormal ureter morphology *1.52e-04

$-\log_{10}$(p-value)

(c)

Mouse 367 Oligo up
Mouse 366 Oligo up
Mouse 365 Oligo up
Mouse 368 Oligo up
Mouse 364 Oligo up

$-\log_2$(p value)

Allen Brain Atlas 10X scRNA

(b)

Probeset ID	Gene Symbol	Fold-Change	p-value
1452595_at	Adamts4	-1.61	3.8170E-03
1455965_at	Adamts4	-1.57	9.8112E-04
1433543_at	Anln	-2.05	3.5341E-04
1439648_at	Anln	-1.44	1.2762E-03
1418472_at	Aspa	-1.79	9.8857E-04
1418922_at	Cadm3	-1.30	2.6426E-02
1416003_at	Cldn11	-1.51	3.3132E-02
1449296_a_at	Cnp	-1.48	8.3001E-03
1418980_a_at	Cnp	-1.43	7.1520E-03
1437341_x_at	Cnp	-1.35	8.9037E-03
1415798_at	Ddr1	-1.56	2.6742E-02
1448619_at	Dhcr7	-1.30	2.4602E-02
1426314_at	Ednrb	-1.36	3.7412E-03
1423594_a_at	Ednrb	-1.53	8.4106E-03
1437347_at	Ednrb	-1.45	1.7875E-02
1456530_x_at	Elovl1	-1.60	3.6945E-02
1440902_at	Ermn	-3.87	5.4679E-03
1436578_at	Ermn	-2.85	1.3364E-03
1426960_a_at	Fa2h	-1.94	8.0495E-03
1423418_at	Fdps	-1.77	3.6498E-04
1454078_a_at	Gal3st1	-1.59	2.8567E-03
1448766_at	Gjb1	-2.65	1.6514E-03
1448767_s_at	Gjb1	-1.79	6.4566E-03
1450483_at	Gjc2	-1.94	6.5479E-03
1450875_at	Gpr37	-2.23	5.9776E-03
1456312_x_at	Gsn	-2.11	1.4828E-02
1436991_at	Gsn	-2.08	7.5055E-03
1415812_at	Gsn	-2.05	1.6802E-02
1437171_x_at	Gsn	-1.92	2.6341E-02
1433446_at	Hmgcs1	-1.32	1.4642E-02
1437401_at	Igf1	-1.48	3.3315E-03
1434413_at	Igf1	-1.45	2.9371E-03
1454159_a_at	Igfbp2	-1.54	2.1745E-03
1452114_s_at	Igfbp5	-1.53	2.3838E-02
1417933_at	Igfbp6	-1.98	5.3222E-03
1416304_at	Litaf	-1.53	7.3165E-05
1416303_at	Litaf	-1.39	2.4227E-03
1460219_at	Mag	-1.53	2.2192E-02
1417275_at	Mal	-1.91	2.9800E-02
1432558_a_at	Mal	-1.86	3.1420E-02
1421010_at	Mobp	-1.80	1.1494E-04
1433785_at	Mobp	-1.79	9.7242E-04
1450088_a_at	Mobp	-1.78	9.3809E-04
1436263_at	Mobp	-1.69	4.1936E-03
1448768_at	Mog	-2.46	6.9939E-03
1423413_at	Ndrg1	-1.86	2.7192E-02
1456174_x_at	Ndrg1	-1.81	1.6614E-02
1420760_s_at	Ndrg1	-1.56	1.6392E-02
1450976_at	Ndrg1	-1.53	1.4751E-02
1450977_s_at	Ndrg1	-1.45	1.4419E-02
1435854_at	Opalin	-1.65	1.5470E-03
1421916_at	Pdgfra	-1.35	4.4552E-02
1448558_a_at	Pla2g4a	-1.40	4.0122E-05
1425468_at	Plp1	-1.42	1.4636E-02
1425467_a_at	Plp1	-1.41	7.2759E-03
1427019_at	Ptprz1	-1.38	2.5851E-02
1436989_s_at	Slc12a6	-1.45	5.8150E-03
1419064_at	Ugt8a	-1.97	1.5863E-03
1419063_at	Ugt8a	-1.79	1.9440E-03

(d)

Ctrl $Atrx^{FoxG1cre}$

MOG
Ctx   Ctx
CC   CC

MBP
Ctx   Ctx
CC   CC

(e)

C1 K1 C2 K2 C3 K3 C4 K4

MAG .... 100 kDa

MOG .... 25 kDa

MBP .... 21 kDa
                     18 kDa
                     17 kDa

Actin .... 42 kDa

(f)

MAG
*
Relative protein expression
Ctrl $Atrx^{Foxg1cre}$

MOG
*
Relative protein expression
Ctrl $Atrx^{Foxg1cre}$

MBP
*
Relative protein expression
Ctrl $Atrx^{Foxg1cre}$

Fig. 1 | Defective myelination in the ATRX-null mouse forebrain. a Microarray analysis of P17 control and $Atrx^{FoxG1Cre}$ forebrain reveals a significant downregulation ($P < 0.05$) of genes related to myelination and oligodendrocyte morphology ($n = 3$ animals for each genotype). **b** List of genes corresponding to the "Abnormal Myelination" category, along with fold changes and p-values. **c** Manhattan plot of Allan Brain Atlas 10X scRNA gene set enrichment from the list of downregulated genes. Each line on the x-axis denotes a single gene set and the y-axis measures the $-\log_{10}$(p-value) for each gene set. **d** Immunofluorescence microscopy of P20 brain cryosections stained with anti-MOG (green) and anti-MBP (red) antibodies confirms decreased levels of these myelin proteins in the cortex (Ctx) and corpus callosum (CC) of the forebrain of $Atrx^{FoxG1Cre}$ mice compared to controls (Ctrl) ($n = 3$ animals for each genotype). Scale bar, 500 μm. **e, f** Western blot analysis of P20 forebrain protein extracts showing significantly decreased levels of MAG ($p = 0.0006$), MOG ($p = 0.0286$) and MBP ($p = 0.0009$) in $Atrx^{FoxG1Cre}$ compared to control mice ($n = 4$ animals for each genotype) after normalization to β-actin protein levels. Data are presented as mean values +/− SEM and asterisks indicate $p < 0.05$ (Two-sided Student's T-test). Source data are provided as a Source Data file.

not clear whether this effect is cell autonomous in OPCs or caused by ATRX loss in other cell types that provide trophic support to OPCs. To resolve whether ATRX regulates myelination intrinsically in OPCs or indirectly via neuronal signaling (or both), we generated mice that lack ATRX in forebrain excitatory neurons using the *NexCre* driver mice for $Atrx^{loxP}$ recombination[53]. We confirmed the absence of ATRX nuclear protein in cortical neurons by co-immunofluorescence staining of ATRX and the neuronal marker NeuN (Fig. S1a). We next examined myelin protein expression in the forebrain by immunofluorescence staining of P20 brain cryosections and no obvious difference in MBP and MOG protein was observed between control and $Atrx^{NexCre}$ mice (Fig. S1b). Furthermore, MAG, MOG and MBP protein levels were
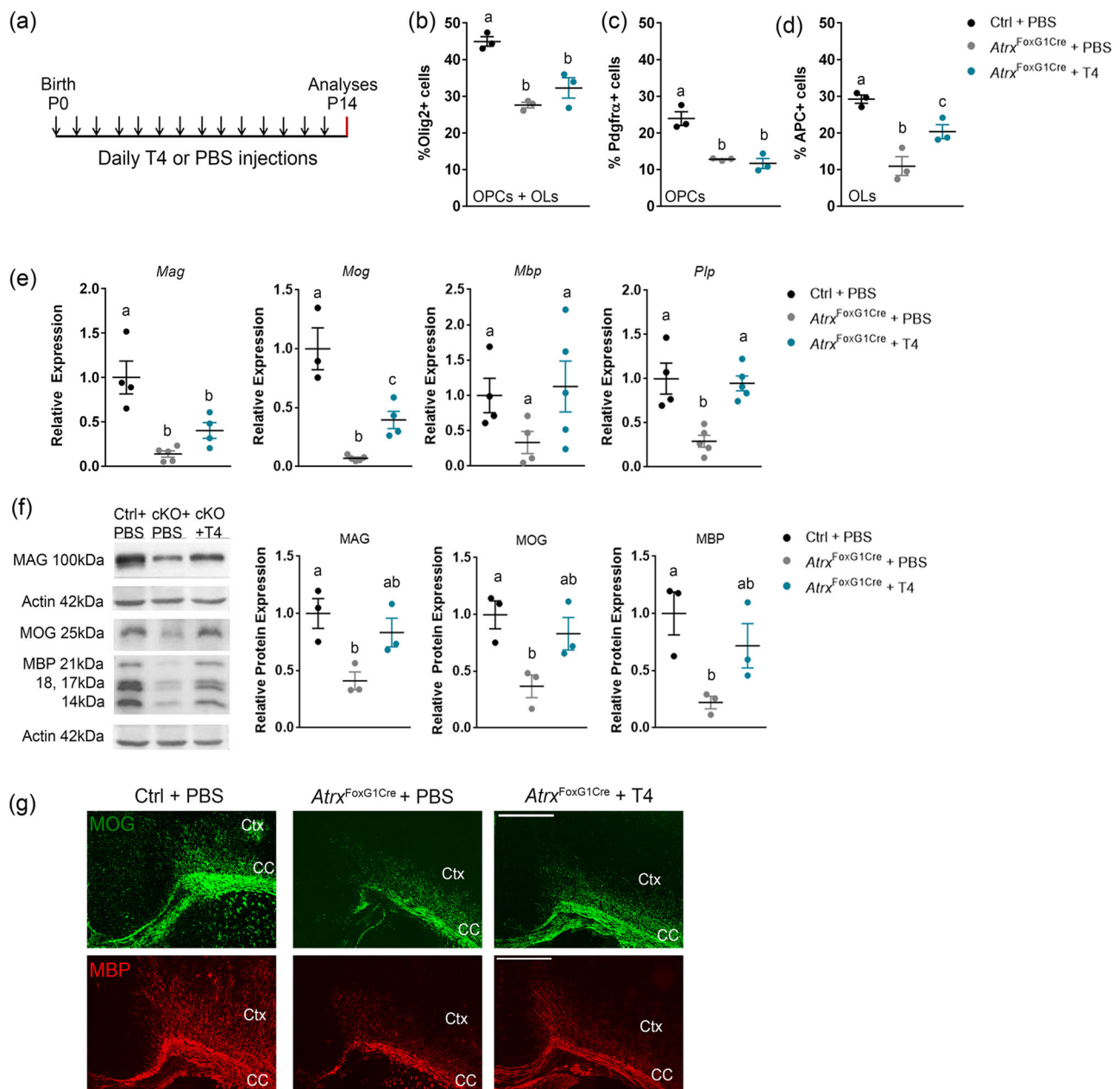
Fig. 2 | Postnatal thyroxine treatment partially replenishes the number of APC + OLs and the expression of myelin proteins in the ATRX-null forebrain but does not restore the number of Pdgfrα + OPCs. a Outline of experimental design. Each arrow represents a subcutaneous (SC) injection of 0.1 mg/kg T4 or PBS to *Atrx*^{FoxG1Cre} and control pups. Analyses were then performed at P14. Quantification of immunostained P14 cryosections demonstrates that the reduced number of **b** Olig2+ (*p* = 0.0013) and **c** Pdgfrα+ cells (*p* = 0.0026) observed in the *Atrx*^{FoxG1Cre} mice is not rescued by T4 treatment (Olig2+ *p* = 0.0064, Pdgfrα+ *p* = 0.0016; *n* = 3 animals for each genotype). **d** The number of APC+ cells are partially rescued upon T4 treatment (*p* = 0.0435; *n* = 3 animals for each genotype). **e** qRT-PCR shows that transcript levels of several myelin genes are decreased in the P14 *Atrx*^{FoxG1Cre} forebrain and partially restored following T4 treatment (*Mag* Ctrl *n* = 4, *Atrx*^{FoxG1Cre} + PBS *n* = 5, *Atrx*^{FoxG1Cre} + T4 *n* = 4; *Mog* Ctrl *n* = 3, *Atrx*^{FoxG1Cre} + PBS *n* = 5, *Atrx*^{FoxG1Cre} + T4

n = 4; *Mbp* Ctrl *n* = 4, *Atrx*^{FoxG1Cre} + PBS *n* = 5, *Atrx*^{FoxG1Cre} + T4 *n* = 5; *Plp* Ctrl *n* = 4, *Atrx*^{FoxG1Cre} + PBS *n* = 5, *Atrx*^{FoxG1Cre} + T4 *n* = 5 animals for each genotype). **f** Western blot analysis of MAG, MOG and MBP shows decreased protein levels in P14 *Atrx*^{FoxG1Cre} compared to control forebrain extracts (MAG *p* = 0.0247, MOG *p* = 0.0261, MBP *p* = 0.0307) and partial rescue upon T4 treatment (MAG *p* = 0.5838, MOG *p* = 0.6298, MBP *p* = 0.4642; *n* = 3 animals for each genotype), normalized to β-actin protein levels. **g** Immunofluorescence staining of P14 brain cryosections highlights the decreased expression of MOG (green) and MBP (red) protein levels in the *Atrx*^{FoxG1Cre} cortex (Ctx) and corpus callosum (CC) that are ameliorated following T4 treatment (*n* = 3 animals for each genotype). Scale bar, 500 μm. Data are presented as mean values +/− SEM, and groups with different letters significantly differ from one another. All data were analyzed by one-way ANOVA with post-hoc Tukey HSD. Source data are provided as a Source Data file.

equivalent to controls when assessed by immunoblot of P20 *Atrx*^{NexCre} forebrain extracts (*n* = 3 each genotype; Student's *T*-test, MAG *p* = 0.627; MOG *p* = 0.917, MBP *p* = 0.425) (Fig. S1c). These results establish that ATRX is not required in neurons of the developing brain for proper signaling to OPCs and for normal production of myelin.

Loss of ATRX in OPCs leads to hypomyelination
We first verified that ATRX is expressed in OPCs and OLs in the mouse brain by co-staining of ATRX with PDGFRα and APC, respectively (Fig. S2). Next, we targeted ATRX deletion in primitive OPCs (priOPCs) and OPCs using the tamoxifen-inducible *Sox10CreER*^{T2} mice, which
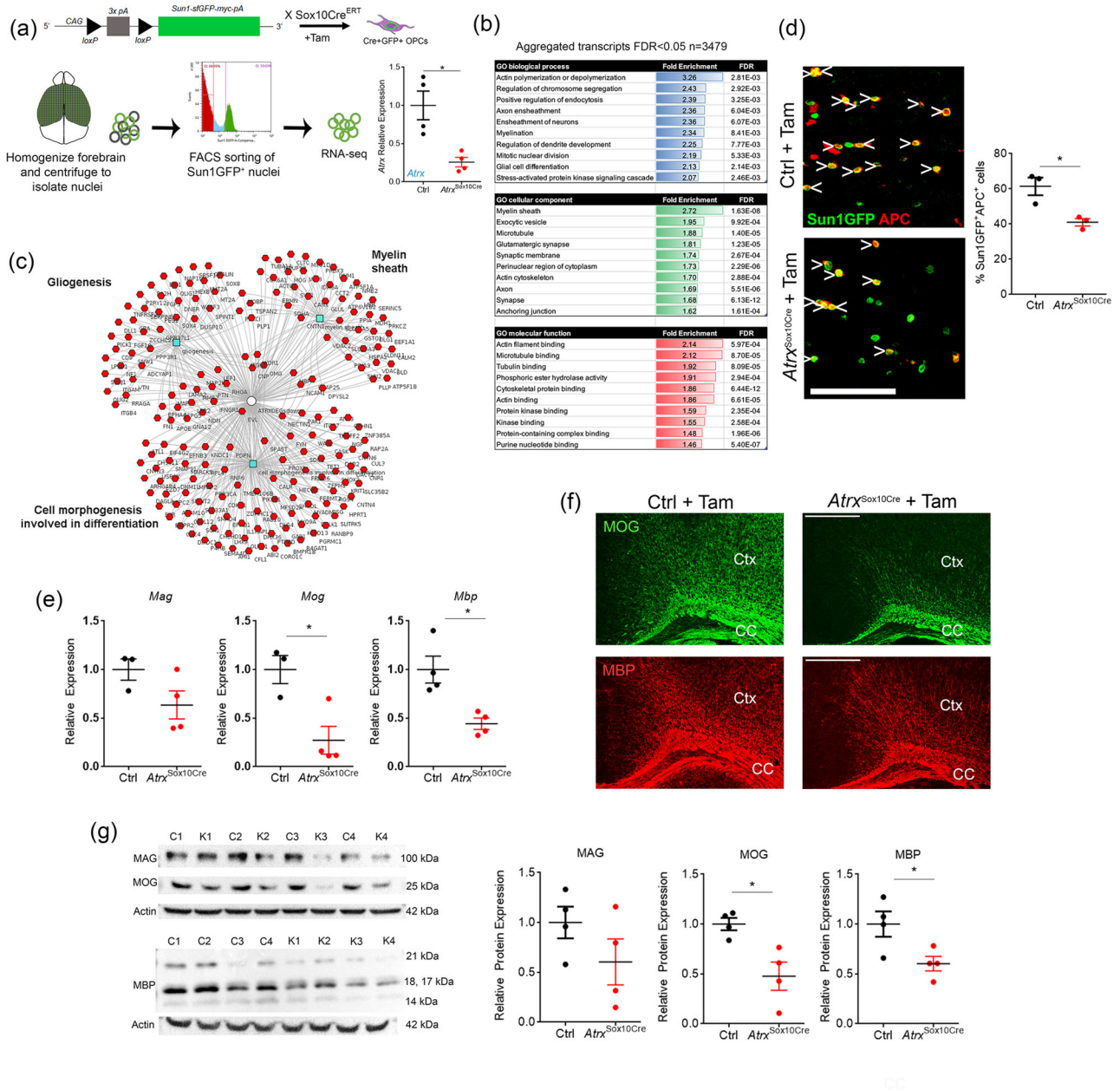
Fig. 3 | Defective differentiation of ATRX-null OPCs causes hypomyelination.
a Sun1GFP⁺ nuclei were sorted and used for RNA-sequencing. RT-qPCR analysis of Sun1GFP⁺ sorted nuclei demonstrates reduced *Atrx* expression ($p = 0.0096$ $n = 4$ animals for each genotype). **b** Gene Ontology pathway analysis of significantly altered genes identified by RNA-sequencing ($n = 3$ animals for each genotype). **c** Cluster analysis of downregulated genes in $Atrx^{Sox10Cre}$ OPC/OL compared to control nuclei are related to cell differentiation, gliogenesis and the myelin sheath. **d** Cell counts show significantly fewer Sun1GFP+ cells co-staining with the mature OL marker APC (red) in the P20 $Atrx^{Sox10Cre}$ corpus callosum compared to controls. Scale bar, 100 μm ($p = 0.00196$, $n = 3$ animals for each genotype). **e** RT-qPCR analysis shows reduced expression of *Mag* ($p = 0.1028$), *Mog* ($p = 0.0174$) and *Mbp* ($p = 0.0100$) in $Atrx^{Sox10Cre}$ P35 optic tract compared to controls (*Mag* Ctrl $n = 3$,

$Atrx^{Sox10Cre}$ $n = 4$; *Mog* Ctrl $n = 3$, $Atrx^{Sox10Cre}$ $n = 4$; *Mbp* $n = 4$ animals for each genotype). **f** Immunofluorescence staining reveals that myelin proteins MOG (green) and MBP (red) are reduced in P20 $Atrx^{Sox10Cre}$ cortex (Ctx) and corpus callosum (CC) compared to controls ($n = 3$ animals for each genotype). Scale bar, 500 μm. **g** Western blot analysis of MAG ($p = 0.2075$), MOG ($p = 0.0149$) and MBP ($p = 0.0357$) and quantification (right) confirms decreased expression of these proteins in P20 $Atrx^{Sox10Cre}$ mouse forebrain protein extracts compared to controls after normalization to β-actin ($n = 4$ animals for each genotype). Data are presented as mean values +/− SEM. All data were analyzed by two-sided Student's *T*-test; asterisks indicate significance of p < 0.05. The figure was partly generated using Servier Medical Art, provided by Servier, licensed under a Creative Commons Attribution 3.0 unported license. Source data are provided as a Source Data file.

upon mating with $Atrx^{LoxP}$ mice produce $Atrx^{Sox10-iCreERT2}$ ($Atrx^{Sox10Cre}$) mice[54]. The Cre-sensitive nuclear membrane *Sun1GFP* reporter was also introduced to allow fate tracking of Cre-expressing cells (Fig. 3a)[55]. Cre recombination was induced by daily intraperitoneal (IP) injection of nursing dams for three successive days (pups at P1-P3)[56] and the mice were analyzed at P20 (Fig. 3a). *Atrx* depletion was confirmed by isolating nuclei from control and $Atrx^{Sox10Cre}$ P20 forebrains and sorting

the Sun1GFP⁺ OPC nuclei. qRT-PCR analysis confirmed a 74.2% decrease in *Atrx* transcript levels in $Atrx^{Sox10Cre}$ Sun1GFP⁺ nuclei compared to control Sun1GFP⁺ nuclei ($n = 4$ each genotype; Student's *T*-test, $p = 0.0096$) (Fig. 3a).

We next performed RNA-seq of Sun1GFP+ nuclei obtained from control and $Atrx^{Sox10Cre}$ forebrain and identified 3479 altered genes (aggregated transcripts, Lancaster method, p value < 0.05). Gene

ontology analysis identified categories of enrichment for biological processes "myelination", "axon ensheathment" and "ensheathment of neurons", as well as "glial cell differentiation" and "actin polymerization and depolymerization". Moreover, the top cellular component category of enrichment was "myelin sheath" and many of the molecular function enrichment categories featured aspects of cytoskeletal biology, possibly reflecting extensive changes in cell shape and membrane architecture during myelination (Fig. 3b). Cluster analysis of only the downregulated genes further emphasized that numerous genes implicated in myelination, gliogenesis and cell morphogenesis involved in differentiation are downregulated in ATRX-null priOPCs and their progeny (Fig. 3c).

To verify potential defects in OPC differentiation and myelination, we performed immunofluorescence staining for APC, a marker of differentiated but immature OLs (iOLs) in P20 control and $Atrx^{Sox10Cre}$ cortical sections. There was a significant reduction in the number of Sun1GFP+ ATRX-null cells that co-expressed APC (41%) compared to Sun1GFP+ control cells (61.4%) (Fig. 3d) ($n = 3$ each genotype; $p = 0.020$ Student's T-test), indicating a lower number of differentiating iOLs. RNA transcripts of mature OLs (mOL)-specific genes Mag, Mog, Mbp were also significantly decreased in P35 $Atrx^{Sox10Cre}$ optic tract ($n = 3-4$ each genotype; Mag $p = 0.10$, Mog $p = 0.017$, Mbp $p = 0.010$ Student's T-test) (Fig. 3e). Furthermore, immunofluorescence staining for MOG and MBP in brain cryosections at P20 showed decreased level of these myelin proteins in the corpus callosum and cortex of $Atrx^{Sox10Cre}$ mice compared to controls (Fig. 3f). Reduced myelin protein expression in $Atrx^{Sox10Cre}$ mice was confirmed by western blot analysis of MAG, MOG and MBP ($n = 4$ each genotype; MAG $p = 0.21$, MOG $p = 0.015$, MBP $p = 0.036$ Student's T-test) (Fig. 3g). These results demonstrate that ATRX-null priOPCs/OPCs have a reduced capacity to differentiate into iOLs and mOLs, leading to reduced myelination.

Loss of the Olig2 fate specification factor in ATRX-null cells

At all stages of development, priOPCs, OPCs and OLs express Olig2, an essential regulator of OL lineage specification[3,57,58]. Olig2 suppresses astrocytic fate[5-7] and promotes OL differentiation via regulation of the chromatin remodelling complex Smarca4/Brg1[10]. The absence of ATRX protein was confirmed in $Atrx^{Sox10Cre}$ OPCs by immunofluorescence staining and imaging in parallel with the Sun1GFP reporter (Fig. 4a). Upon staining the $Atrx^{Sox10Cre}$ corpus callosum with Olig2 to confirm specific deletion in the oligodendrocyte lineage cells, we were surprised to see that a large proportion of Sun1GFP+ ATRX-null cells did not express Olig2 (40.5%) compared to Sun1GFP+ control OPCs (12.6%) ($n = 3-4$ each genotype; Student's T-test, $p = 0.013$, Fig. 4b, c). Similarly, qRT-PCR of RNA isolated from sorted $Atrx^{Sox10Cre}$ Sun1GFP+ nuclei confirmed a 57% reduction in $Olig2$ transcripts compared to Sun1GFP+ control nuclei ($n = 3-4$ each genotype; Student's T-test, $p = 0.036$) (Fig. 4d).

Loss of $Olig2$ expression in ATRX-null cells was also observed in primary glial cell cultures. Cre-mediated recombination was induced by administration of tamoxifen to nursing dams for two days (age of pups P0-P1). P3 cortices of $Atrx^{Sox10Cre}$ or control mice that also express the Ai14-TdTomato reporter[59] were dissociated and cells grown in mixed glial co-culture in which OPCs are expanded on top of an astrocyte monolayer (Fig. 4e)[60,61]. Immunofluorescence staining revealed that many ATRX-null Ai14+ cells do not express Olig2 after 5, 6 and 9 days in vitro (DIV) (Fig. 4 f, g) and that these cells appear elongated and flattened instead of the typical rounded shape of OPCs (Fig. 4f, h). We also detected a significant increase in apoptosis of Ai14+ ATRX-null rounded OPCs compared to control cells at both DIV5 and DIV6 (Fig. 4i, j). Ki67 staining showed that the same proportion of rounded Ai14+ cells proliferate in the presence or absence of ATRX at DIV5. However, a significant decrease in Ai14 +/Ki16+ cells was detected at DIV6 (Fig. S3). Overall, these results demonstrate that a subset of ATRX-null OPCs lack Olig2 expression and either undergo apoptosis or

change morphology. In addition, the proliferation of ATRX-null OPCs was not initially affected but was decreased by 6 DIV compared to control cells.

ATRX co-occupies the Olig2 locus with other OPC fate regulators and promotes an active chromatin state

We next performed ATRX chromatin immunoprecipitation on cultured primary mouse OPCs and identified 42,820 ATRX peaks using MACS2[62], with the bulk of ATRX chromatin occupancy identified two highly represented DNA motifs corresponding to Oct6 ($Pou3f1$) and Brn1 ($Pou3f3$) (Fig. 5b) from ChIP-seq data previously done in NPCs[63]. These transcription factors are not known to contribute to OPC identify or differentiation and their expression may not be substantial in OPCs. Not surprisingly, when we compared ATRX enrichment +/−3 kb from Oct6 and Brn1 binding site midpoints in OPCs, we only observed weak ATRX enrichment flanking these transcription factor binding sites. Interestingly, ATRX binding was more evident at Sox2 peaks, which was analyzed in parallel, as a control (Fig. 5c). These results suggest that in OPCs, ATRX may be co-binding chromatin with a POU domain transcription factor that has yet to be identified.

We then turned to other established critical factors involved in OPC differentiation, including HDAC3[64], CHD7[65], CHD8[66,67] and OLIG2[3,58,68], for which data was available for comparison. Comparing ChIP-seq of ATRX and these factors in OPCs showed substantial co-occupancy of ATRX with chromatin remodelers CHD7 and CHD8, but not with HDAC3 or OLIG2 (Fig. 5d, f). CHD7 and CHD8 are ATP-dependent chromatin remodeling proteins involved in OL differentiation and myelination[65,66]. CHD8 has been implicated in the establishment of OPC identity, while both CHD7 and CHD8 target enhancers of key myelinogenic genes[65], which are marked by histone H3 acetylated at lysine 27 (H3K27Ac)[69]. Comparison of H3K27Ac ChIP-seq peaks from OPCs, immature OLs (iOLs) and mature OLs (mOLs) revealed elevated ATRX binding at active enhancers in these cell types, although it was more pronounced in OPCs compared to iOLs and mOLs (Fig. 5e, f). ATRX directly binds the $Olig2$ gene locus at regulatory sites defined by H3K27Ac and CHD8, but not for CHD7 (Fig. 5g). An overlap of ChIP-seq peaks between ATRX, H3K27Ac and CHD8 is also observed at numerous other genes involved in OL fate specification and differentiation, such as $Nkx2-2$, $Sox8$, $Thra$ and Mbp (Fig. S4). Given the strong association between H3K27Ac and ATRX, we performed ChIP-qPCR of H3K27Ac in control and $Atrx^{Sox10Cre}$ optic nerves. The results demonstrate a significant reduction of this histone post-translational modification at the $Olig2$ gene locus in the absence of ATRX, corresponding to reduced gene expression (Fig. 5h).

We further compared the list of differentially expressed genes identified by RNA-seq, to cell type-specific gene lists[70] and determined that the majority of downregulated genes are highly expressed not only in OLs, but also OPCs, suggesting that perhaps OPC determination is compromised in the absence of ATRX (Fig. 6a). In addition to Olig2, several other transcription factors involved in OPC fate[71] were downregulated according to RNA-seq data, including $Olig1$, $Sox8$, and $Zfp36l1$ (Fig. 6b). The latter codes for a transcription factor that promotes differentiation of multipotent progenitors into pri-OPCs[71] suggesting that ATRX-null cells fail to express early determinants of OPC and pri-OPC identify. Indeed, RT-qPCR analysis shows a reduction in the expression of the OPC markers $Pdgfr\alpha$, $Cspg4$ (NG2) and $Gpr17$ ($n = 3-4$ each genotype; Student's T-test, $Pdgfr\alpha$ $p = 0.017$, $Cspg4$ $p = 0.032$, $Gpr17$ $p = 0.0004$) in the $Atrx^{Sox10Cre}$ mice as compared to controls (Fig. 6c). The priOPC-expressed genes $Olig1$ and $Sox10$ were similarly reduced at the transcript level but did not reach the significance threshold of $p < 0.05$ (Fig. 6c) ($n = 3$ each genotype; $Olig1$ $p = 0.081$, $Sox10$ $p = 0.133$ Student's T-test). Moreover, Sun1GFP+ ATRX-null OPCs in the corpus callosum stain less frequently for PDGFRα (24.9%) compared to controls (41.1%) (Fig. 6d, e) ($n = 3$ each genotype; $p = 0.001$, Student's T-test). Immunofluorescence staining
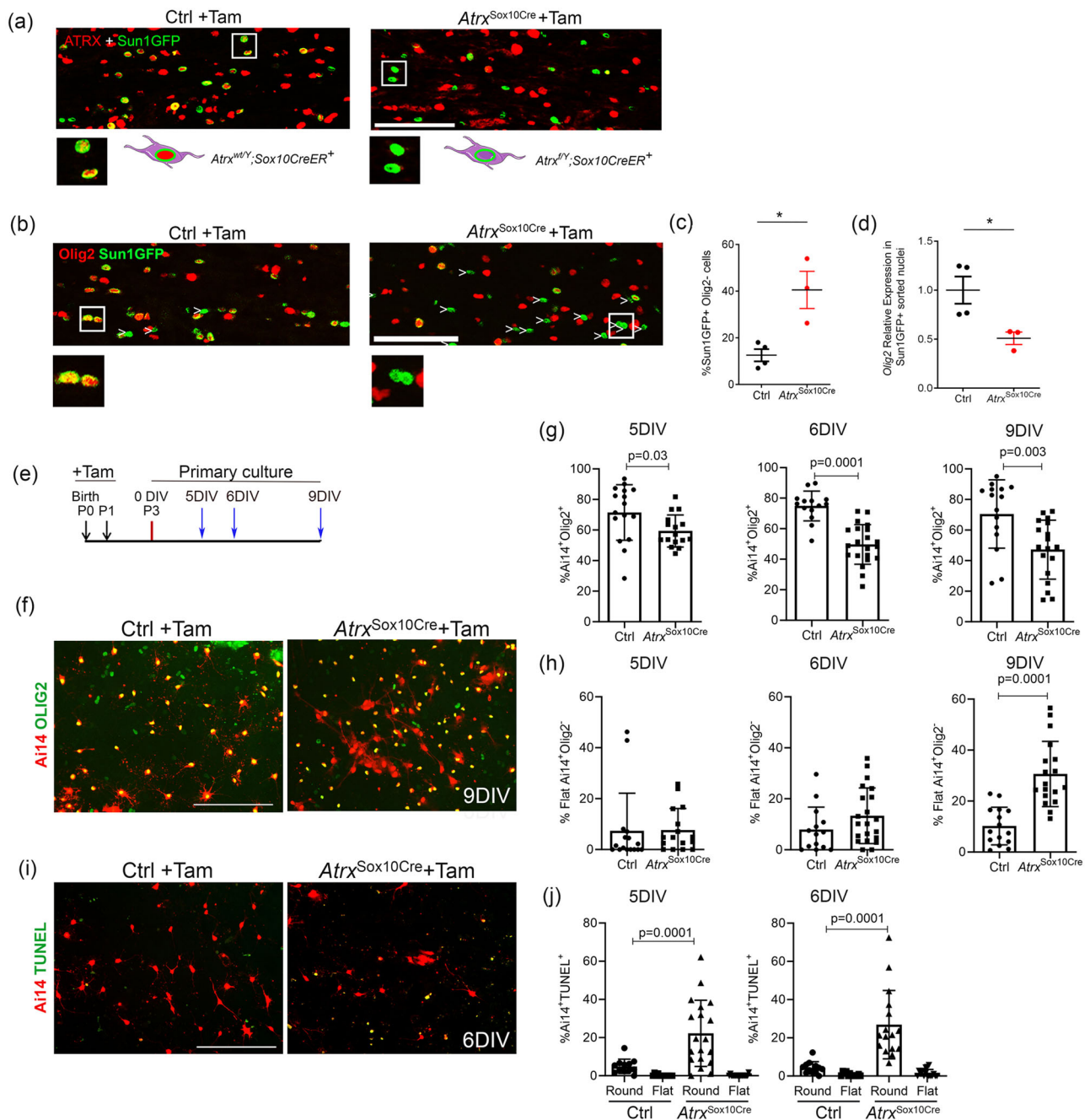
Fig. 4 | Loss of Olig2 expression and morphological changes in a subset of ATRX-null OPCs. a Immunofluorescence microscopy of P20 $Atrx^{Sox10Cre}$ corpus callosum shows expression of the Sun1GFP fusion protein in the nuclear membrane of OPCs upon tamoxifen treatment (left). P20 $Atrx^{Sox10Cre}$ treated with tamoxifen also express Sun1GFP but lack expression of nuclear ATRX (right) ($n = 3$ animals for each genotype). Scale bar, 100 μm. **b** Fate mapping of ATRX-null Sun1GFP$^+$ OPCs reveals frequent loss of the Olig2 transcription factor (white arrowheads). Scale bar, 100 μm. **c** Quantification of Sun1GFP$^+$ OPCs that lack Olig2 staining ($p = 0.0127$ Ctrl $n = 4$, $Atrx^{Sox10Cre}$ $n = 3$ animals for each genotype). Data are presented as mean values +/– SEM. **d** qRT-PCR analysis demonstrates significantly decreased $Olig2$ transcripts in Sun1GFP$^+$ $Atrx^{Sox10Cre}$ sorted nuclei compared to Sun1GFP$^+$ control nuclei ($p = 0.0359$, Ctrl $n = 4$, $Atrx^{Sox10Cre}$ $n = 3$ animals for each genotype). **e** Experimental timeline of tamoxifen (Tam) injections to nursing mothers at P0 and P1 (black arrows). **f** Images of Ai14 control and $Atrx^{Sox10Cre}$ mixed glial culture stained for Olig2 (green) at 9DIV. Scale bar, 200 μm. **g** The proportion of Ai14$^+$Olig2$^+$ cells is lower in ATRX-null cultures at DIV5 ($p = 0.0282$, $n = 16$ images scored for cultures established from 4 animals of each genotype), DIV6 ($p = 0.0001$, Ctrl $n = 14$ images for 4 animals, $Atrx^{Sox10Cre}$ $n = 21$ images for 4 animals) and DIV9 ($p = 0.003$, Ctrl $n = 15$

images scored for cultures established from 3 animals, $Atrx^{Sox10Cre}$ $n = 18$ images for 3 animals). Data are presented as mean values +/– SD. **h** The percent of Ai14$^+$Olig2$^-$ ATRX-null OPCs exhibiting a flattened morphology increases over time in culture, reaching significance at DIV9 ($p = 0.0001$, Ctrl $n = 15$ images scored from cultures established for 3 animals, $Atrx^{Sox10Cre}$ $n = 18$ images for 3 animals). Data are presented as mean values +/– SD. **i** Images of Ai14 control and $Atrx^{Sox10Cre}$ mixed glial cultures at 6DIV stained for TUNEL (green). Scale bar, 200 μm. **j** Quantification of TUNEL staining shows increased cell death of round-shaped ATRX-null OPCs at DIV5 ($p = 0.0001$, Ctrl $n = 12$ images scored from cultures established from 3 animals, $Atrx^{Sox10Cre}$ $n = 19$ images scored for 4 animals) and DIV6 ($p = 0.0001$, Ctrl $n = 12$ images scored for 3 animals, $Atrx^{Sox10Cre}$ $n = 16$ images scored for 3 animals). Data are presented as mean values +/– SD. All graphs with two groups were analyzed by two-sided Student's T-test; asterisks indicate $p < 0.05$. All graphs with four groups were analyzed by one-way ANOVA with post-hoc Tukey HSD. The figure was partly generated using Servier Medical Art, provided by Servier, licensed under a Creative Commons Attribution 3.0 unported license. Source data are provided as a Source Data file.
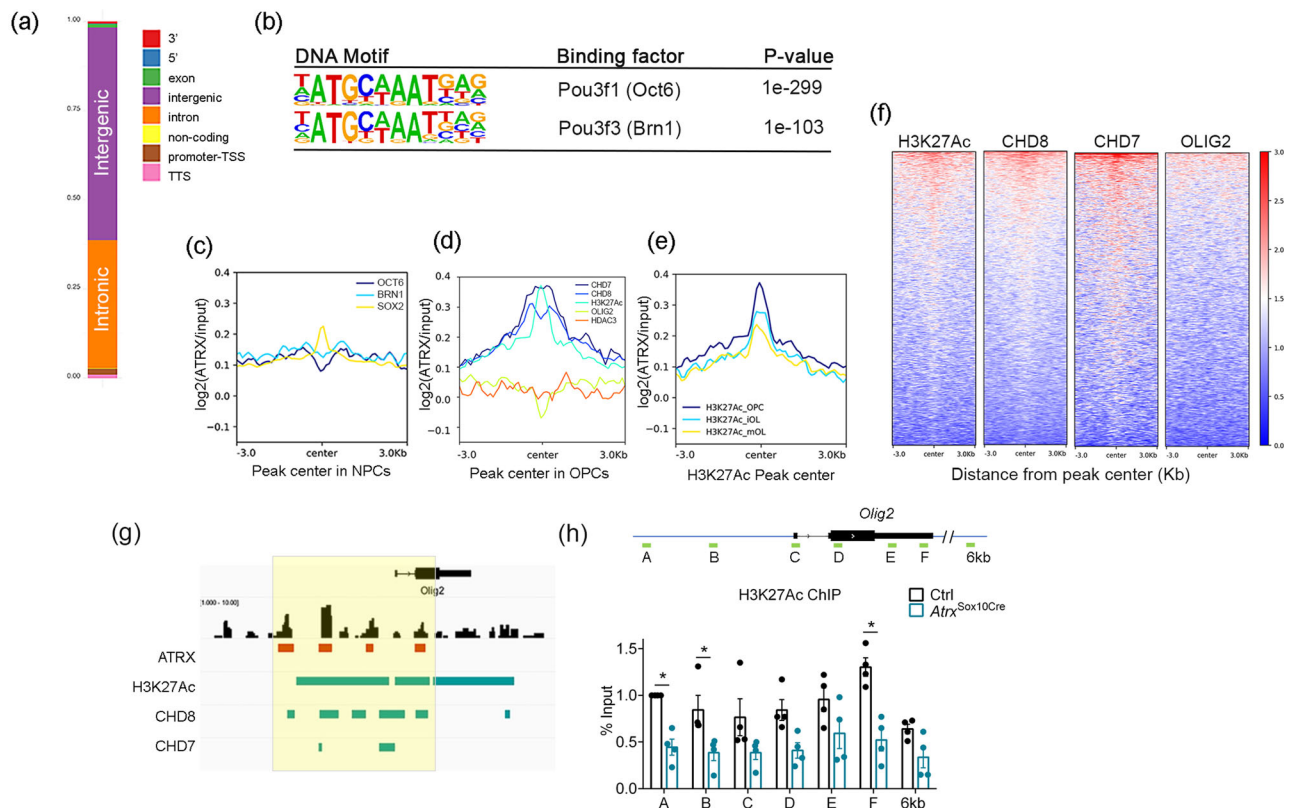
Fig. 5 | ATRX occupancy in OPCs is enriched at active promoters and promotes histone H3K27Ac post-translational modification at the *Olig2* locus. a ATRX ChIP-seq in mouse primary OPCs reveals frequent ATRX binding at intergenic sites and introns (*n* = 1 animal for each genotype). **b** DNA motif enrichment of sequence corresponding to ATRX binding significantly correlate with Oct6 (*p* = 1e-299) and Brn1 (*p* = 1e-103) transcription factor binding sites identified in NPCs. **c** ATRX genome wide occupancy at ChIP-seq peaks of Sox2, Brn1 and Oct6 in NPCs. **d** ATRX occupancy at ChIP-seq peaks of HDAC3, Olig2, CHD7, CHD8 and H3K27Ac in OPCs. **e** C -occurrence of H3K27Ac and ATRX in OPCs, iOLs and mOLs. **f** Heatmaps of ATRX occupancy at ChIP-seq peaks of H3K27Ac, CHD8, CHD7 and OLIG2 in OPCs. **g** IGV view of the *Olig2* gene showing ATRX ChIP-seq peaks (red) and how they align with H3K27Ac, CHD8 and CHD7 (green). **h** ChIP-qPCR of H3K27Ac demonstrates reduced enrichment at several sites at the *Olig2* gene in OPCs the absence of ATRX (A *p* = 0.0097, B *p* = 0.0479, F *p* = 0.0001, *n* = 4 animals for each genotype). Data are presented as mean values +/− SEM; asterisks indicate significance of *p* < 0.05 analyzed by one-way ANOVA with post-hoc Tukey HSD. Source data are provided as a Source Data file.

was also performed on mixed glial cultures to examine OPC development over time. We observed that a significantly decreased proportion of ATRX-null Ai14+ cells express PDGFRα at 6 and 9 DIV compared to control cells and that more Ai14+ cells lack the expression of both SOX10 and OLIG2 at 6 and 9 DIV in *Atrx*[Sox10Cre] compared to control mice (Fig. 6f–h). We conclude that ATRX ablation in postnatal Sox10-expressing priOPCs and OPCs leads to a loss of progenitor identity.

Loss of ATRX leads to ectopic astrogliogenesis

Ablation of the transcription factor Olig2 in OPCs in the postnatal cortex has been reported to induce differentiation into astrocytes[5–7]. This observation, combined with the fact that many ATRX-null OPCs take on an atypical morphology reminiscent of astrocytes in vivo and in vitro, prompted us to investigate whether ATRX-null OPCs adopt a more malleable state conducive to an alternative fate choice. To answer this question, we first compared RNA-seq data to the list of the most enriched genes in astrocytes[70], and found that many astrocyte-enriched genes were upregulated in ATRX-null cells (Fig. 7a). As many of the genes in this list are merely enriched in, but not specific to astrocytes, we then performed immunofluorescence staining of known astrocyte markers in control and *Atrx*[Sox10Cre] brain cryosections at P20. We observed increased S100 calcium-binding protein β (S100β) staining in the corpus callosum and cortex in *Atrx*[Sox10Cre] mice (Fig. 7b). Cells co-expressing the endogenous Sun1GFP and S100β (by immunostaining) were counted, and the results show a 20% increase in the

number of Sun1GFP⁺ cells that co-express S100β in *Atrx*[Sox10Cre] compared to control corpus callosum (*n* = 3 each genotype; Student's *T*-test, *p* = 0.003) (Fig. 7c). S100β can sometimes stain OLs[72] and indeed we observed that a proportion of control Sun1GFP⁺ OPCs express S100β (34.2%). We thus used another well-known astrocyte marker, glial fibrillary acidic protein (GFAP). Like the results obtained for S100β, we observed increased GFAP staining in the cortex of *Atrx*[Sox10Cre] mice (Fig. 7d). Cell counts of GFAP⁺Sun1GFP⁺ cells showed a 15.2% increase in the proportion of Sun1GFP⁺ cells that co-stain with GFAP in *Atrx*[Sox10Cre] compared to control in the corpus callosum (*n* = 3 each genotype; Student's *T*-test, *p* = 0.0074) (Fig. 7e).

Utilizing the Ai14 reporter to assess *Atrx*[Sox10Cre] cell morphology, we could easily see that a subset of ATRX-null Ai14⁺ cells display a highly branched morphology typical of protoplasmic astrocytes as previously observed in *Olig2* knockout mice[6,7]. These cells co-expressed GFAP (Fig. 7f) and the astrocyte specification factor NFIA[73,74] (Fig. 7g) indicating that a subset of ATRX-null cells gained the capacity to at least initiate astrocyte differentiation in vivo. We confirmed this finding in primary glial culture, where at 5 and 6 DIV, significantly more *Atrx*[Sox10Cre] derived cells (Ai14⁺) expressed GFAP compared to control cells (Fig. 7h). Moreover, we observed that many Ai14+ GFAP+ cells lack Olig2 expression in the absence of ATRX (Fig. 7i). These results suggest that a portion of ATRX-null cells initiate an astrocytic differentiation program, instead of the Olig2-driven oligodendrocyte lineage pathway.
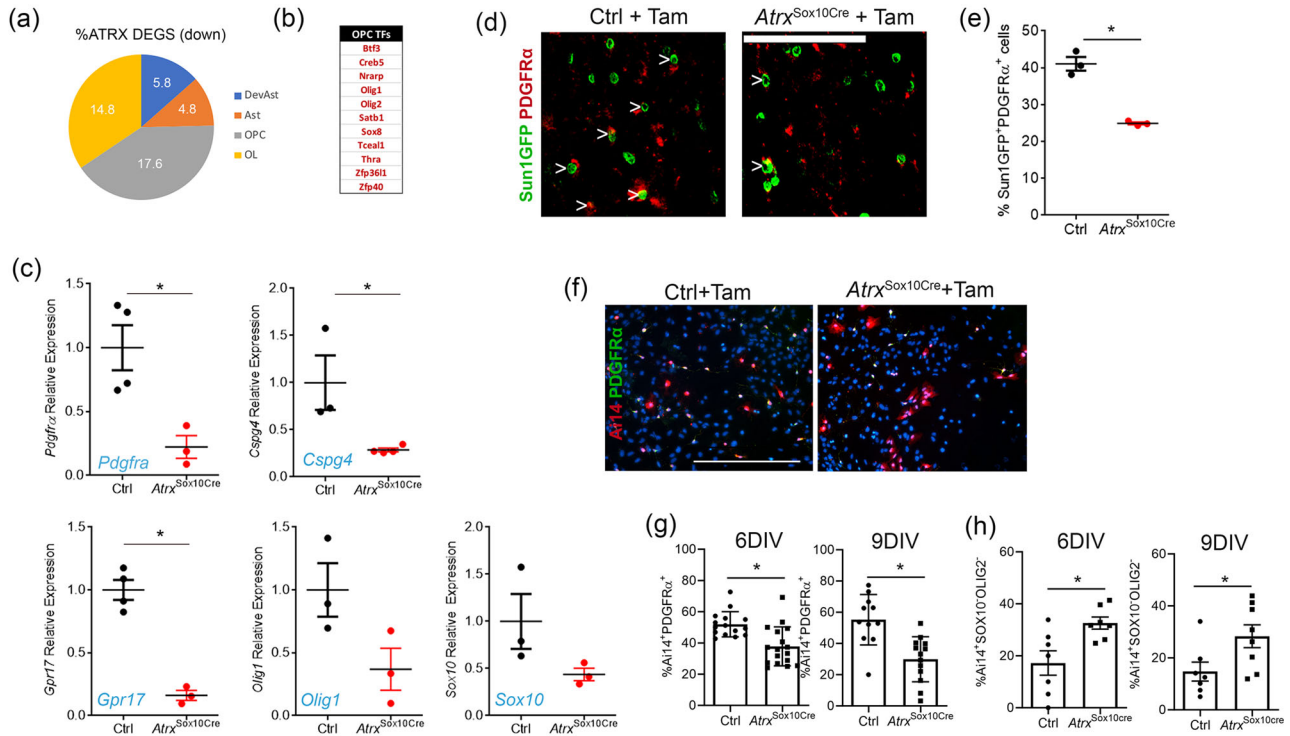
Fig. 6 | Loss of OPC identity upon *Atrx* deletion in Sox10⁺ cells in vivo and in vitro. a Transcriptional analysis of *Atrx*^Sox10Cre sorted Sun1GFP+ nuclei shows that downregulated genes are equally enriched in OLs and OPCs based on data published by Cahoy et al., 2008[70]. **b** Several transcription factors that contribute to OPC fate (Weng et al., 2019)[71] are downregulated upon loss of ATRX. **c** RT-qPCR analysis of Sun1GFP⁺ sorted nuclei demonstrates that key genes that specify OPCs are downregulated in the absence of ATRX (*Pdgfrα* $p = 0.0173$ Ctrl $n = 4$, *Atrx*^Sox10Cre $n = 3$; *Cspg4* $p = 0.0323$ Ctrl $n = 3$, *Atrx*^Sox10Cre $n = 4$; *Gpr17* $p = 0.0004$ Ctrl $n = 4$, *Atrx*^Sox10Cre $n = 3$; *Olig1* $p = 0.081$ $n = 3$; *Sox10* $p = 0.133$ $n = 3$ animals for each genotype). Data are presented as mean values +/− SEM. **d** PDGFRα immunostaining (red) shows decreased proportion of Sun1GFP⁺ PDGFRα⁺ cells in the corpus callosum of tamoxifen-treated *Atrx*^Sox10Cre compared to control mice ($n = 3$ animals for each genotype). Scale bar, 100 μm. **e** Quantification of Sun1GFP⁺ PDGFRα⁺ cells

($p = 0.001$, $n = 3$ animals for each genotype). Data are presented as mean values +/− SEM. **f** Immunostaining of PDGFRα and Ai14⁺ fluorescence at 6DIV. Scale bar, 400 μm. **g** The percentage of Ai14⁺ cells that express PDGFRα at 6DIV ($p = 0.0007$, Ctrl $n = 15$ images scored from cultures established from 3 animals, *Atrx*^Sox10Cre $n = 17$ images scored for 3 animals) and 9DIV ($p = 0.0005$, Ctrl $n = 11$ images scored from cultures established from 3 animals, *Atrx*^Sox10Cre $n = 13$ images scored for 3 animals). Over 1300 Ai14+ cells were counted for each genotype. Data are presented as mean values +/− SD. **h** The percentage of Ai14⁺ cells lacking OLIG2 and SOX10 was quantified in tamoxifen-treated control and *Atrx*^Sox10Cre primary cell culture at 6DIV ($p = 0.0361$, Ctrl $n = 7$ animals, *Atrx*^Sox10Cre $n = 8$ animals) and 9DIV ($p = 0.0127$, $n = 7$ animals). Over 750 Ai14⁺ cells were counted per genotype. Data are presented as mean values +/− SEM. For all graphs, asterisks indicate $p < 0.05$ analyzed by two-sided Student's *T*-test. Source data are provided as a Source Data file.

Discussion

ATP-dependent chromatin remodelers such as Brg1, Brm, CHD7, Chd8 and Ep400 have emerged as critical factors in the regulation of the OL lineage progression and myelination (reviewed in Parras et al. 2020)[75]. Still, many questions remain as to the exact mechanisms by which they exert their effects. In the present study, we add ATRX to the list of chromatin remodelers involved in oligodendrogenesis and report on ATRX-mediated regulation of myelin development through both systemic and cell-autonomous mechanisms. The *Atrx*^FoxG1Cre mice exhibit CNS hypomyelination that can partially be rescued by early postnatal administration of thyroid hormone. Cell type-specific inactivation of ATRX in OPCs, but not in neurons, also resulted in hypomyelination, showing that ATRX loss can have systemic as well as cell-autonomous roles in developmental myelination. We determined that ATRX directly binds to and activates the *Olig2* gene at regulatory sites and promotes an active chromatin state (H3K27Ac). Consequently, Olig2 protein level is reduced in a subset of ATRX-null OPCs, leading to a more permissive precursor state, perhaps through modified chromatin accessibility, allowing for ectopic astrogliogenesis (Fig. 7j).

We first demonstrated that myelination is defective in *Atrx*^FoxG1Cre mice, which have low levels of circulating T4[45,46]. The thyroid hormone receptor is a transcriptional activator for several myelin genes, promoting differentiation of OPCs[23–25]. We observed a significant yet

partial rescue in myelinogenic genes and proteins in *Atrx*^FoxG1Cre mice following T4 supplementation. Whereas the number of APC-positive iOLs increased following T4 administration, the number of PDGFRα-positive OPCs was not restored to control levels. Furthermore, production of Olig2-expressing OPCs in *Atrx*^FoxG1Cre mice was not improved after thyroid hormone treatment, indicating that ATRX may be essential for OPC determination, proliferation or survival involving a mechanism distinct from T4 regulation.

Neuronal communication with OLs is emerging as a key regulator of myelination. Neurons have been proposed to be necessary for adaptive myelination[76,77] and electrical activity from neurons has been shown to induce OPC proliferation and remyelination[78]. ATRX is absent in all cell types of the forebrain of *Atrx*^FoxG1Cre mice, and it was thus conceivable that deletion of *Atrx* in neurons could cause a reduction of the OPC pool and subsequent myelination. Nonetheless, specific deletion of ATRX in neurons did not result in defects in the development of white matter. Conversely, deletion in Sox10-expressing pri-OPCs and OPCs had substantial deleterious effects on myelin production.

Our data indicate that in OPCs, ATRX binds several sites across the *Olig2* gene locus and promotes gene expression partly by helping to promote H3K27Ac via unknown mechanisms. Olig2 is a key determinant of OPC and OL fate, by promoting a cascade of gene expression,
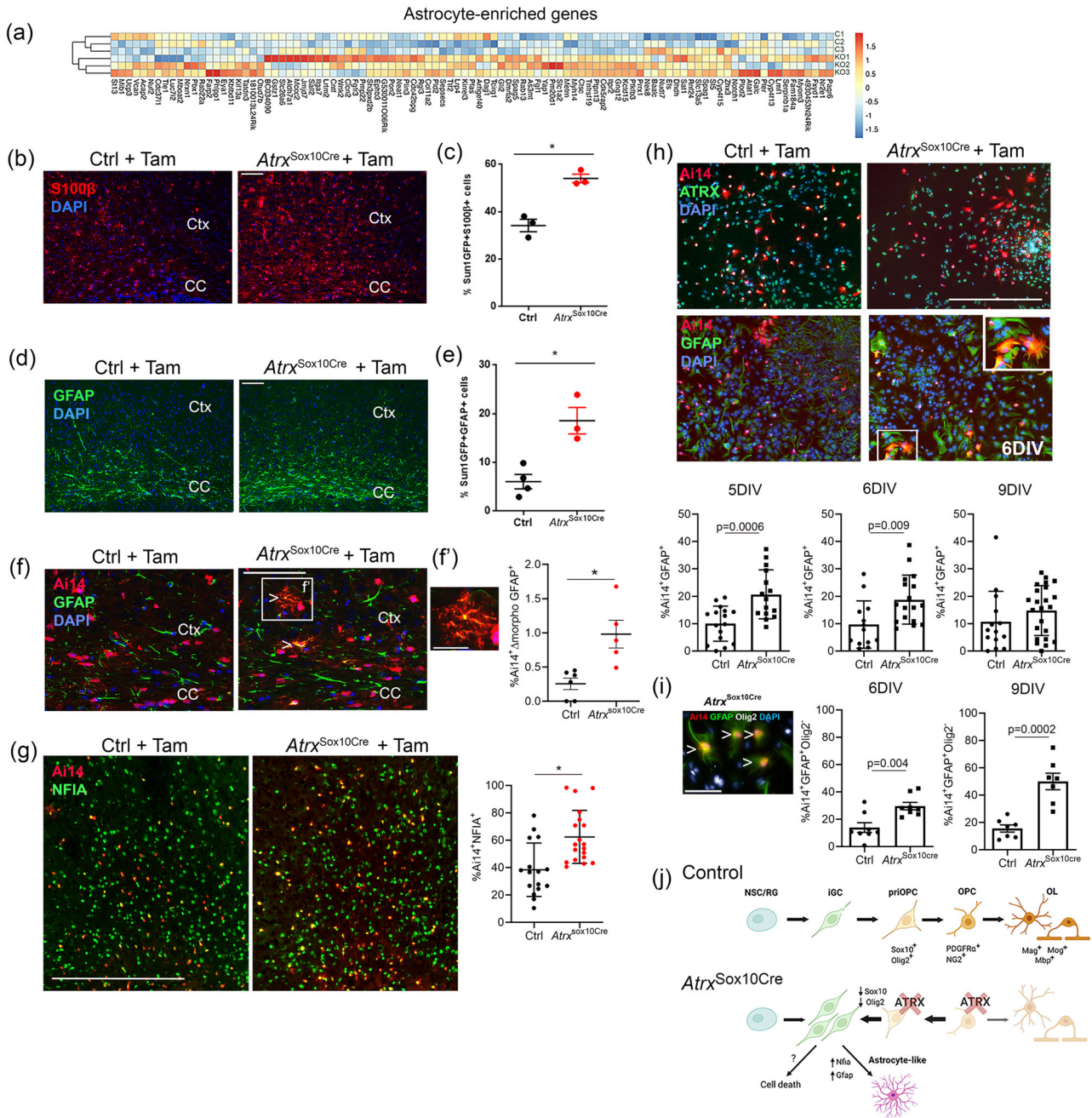
but also by directly suppressing astrocytic fate in conjunction with Olig1[3]. Loss of Olig2 can explain the reduced expression of Pdgfrα, since it is required for induction of this gene in cooperation with Sox10[8,9]. Pdgfrα is essential for OPC proliferation and survival and the decreased expression of this gene might explain the reduced proliferation and increased cell death observed in *Atrx*[Sox10Cre] mixed glial cultures. Depletion of the OPC pool can in turn cause the reduction in myelinating OLs and hypomyelination observed in *Atrx*[Sox10Cre] mice.

The gliogenic switch observed upon loss of ATRX is most likely mediated by changes in the epigenetic and chromatin landscape. Two factors involved in this process are the histone deacetylase HDAC3 and the histone acetylase P300[64]. However, we found no evidence of overlap between the occupancy of ATRX and these two factors in OPCs. Rather, we discovered substantial enrichment of ATRX at H3K27Ac, CHD7 and CHD8 binding sites across the genome. Like ATRX, CHD7 and CHD8 are ATP-dependent chromatin-remodeling enzymes and they can bind to the enhancer regions and near

transcription start sites of myelinogenic genes[65,67]. However, CHD8 expression appears to play a bigger role in OPCs than CHD7. Chromatin occupancy of CHD8 in OPCs is greater than that of CHD7[66], and CHD8 acts upstream of the Brg1-containing BAF complex and Olig2, both of which promote CHD7 expression[67]. Moreover, CHD8 occupancy in OPCs corresponds to proximal enhancer regions marked by H3K27Ac, while this is not the case for CHD7. Based on this, we predict that ATRX co-binds chromatin sites with CHD8 (as opposed to CHD7) in OPCs, although the purpose of utilizing two chromatin remodelers at enhancers will need to be resolved in future studies. It is interesting to note that *CHD8* mutations cause congenital anomalies, intellectual disability and autism accompanied and severe white matter abnormalities[79–81], akin to ATR-X syndrome, suggesting that there might be mechanistic overlap in white matter pathogenesis caused by disruption of these chromatin remodelers.

The fate switch observed upon loss of ATRX is reminiscent of the effects of *Olig2* deletion in the mouse postnatal cortex[6,7]. The timing of

Fig. 7 | A subset of ATRX-null OPCs acquire astrocyte-like features in vivo and in vitro. a Heatmap of astrocyte-enriched genes upregulated in ATRX-null cells, based on Cahoy et al, 2018[70]. **b** Immunostaining of S100β reveals increased levels in the P20 $Atrx^{Sox10Cre}$ corpus callosum (CC) and cortex (Ctx) compared to controls. Scale bar, 100 μm. **c** Number of Sun1GFP+ OPCs that stain positive for S100β ($p = 0.0034$, $n = 3$ animals for each genotype). Data are presented as mean values +/− SEM. **d** Immunostaining of the astrocyte marker GFAP shows increased expression in the P20 $Atrx^{Sox10Cre}$ mouse corpus callosum (CC) and cortex (Ctx) compared to controls. Scale bar, 100 μm. **e** Quantification of the number of Sun1GFP+ OPCs that stain positive for GFAP ($p = 0.0074$, Ctrl $n = 4$, $Atrx^{Sox10Cre}$ $n = 3$ animals of each genotype). Data are presented as mean values +/− SEM. **f** Overlap of the Cre-sensitive Ai14+ reporter (red) and the astrocyte marker GFAP (green) in the $Atrx^{Sox10Cre}$ mouse brain in vivo (white arrowheads). Scale bar, 100 μm. (**f'**) Higher magnification of portion of the image in (**f**), showing GFAP staining in an Ai14+ cell with astrocyte-like morphology. Scale bar, 25 μm. The extent of overlap of GFAP in morphologically altered Ai14+ cells is quantified in the graph on the right ($p = 0.0064$, Ctrl $n = 6$, $Atrx^{Sox10Cre}$ $n = 5$). Data are presented as mean values +/− SEM. **g** Immunostaining of NFIA (green) reveals increased expression in Ai14+ ATRX-null cells. Data is graphed on the right ($p = 0.0009$, Ctrl $n = 16$ images scored from cultures established from 4 animals, $Atrx^{Sox10Cre}$ $n = 19$ images scored for 4 animals.

Data are presented as mean values +/− SD. Scale bar, 400 μm. **h** Images of Ai14 (red) and ATRX (green, top panels) or GFAP (green, bottom panels) in mixed glial cultures at 6DIV. Quantification of Ai14+GFAP+ cells is shown below at DIV5 ($p = 0.0006$, Ctrl $n = 16$ images scored from cultures established from 3 animals, $Atrx^{Sox10Cre}$ $n = 15$ images scored for 3 animals), DIV6 ($p = 0.0092$, Ctrl $n = 13$ images scored for cultures established for 3 animals, $Atrx^{Sox10Cre}$ $n = 17$ images scored for 3 animals) and 9DIV ($p = 0.2268$, Ctrl $n = 14$ images scored for 3 animals, $Atrx^{Sox10Cre}$ $n = 23$ images scored for 4 animals). Data are presented as mean values +/− SD. Scale bar, 400 μm. **i** Co-staining of glial cultures with GFAP (green), Olig2 (white) and DAPI (blue) shows decreased Olig2 staining in GFAP+ Ai14+ ATRX-null cells (white arrowheads), quantified at DIV6 ($p = 0.0035$, $n = 8$ animals) and 9 DIV ($p = 0.0002$, $n = 7$ animals). Data are presented as mean values +/− SEM. Scale bar, 100 μm. **j** Model of the effects of ATRX inactivation in Sox10+ pri-OPCs and OPCs in the mouse postnatal forebrain. Loss of Olig2 and Sox10 expression reverts ATRX-null OPCs and pri-OPCs to multipotent intermediate glial progenitor cells (iGCs), and gain the ability to differentiate into astrocyte-like cells in vitro and in vivo. All data were analyzed by two-sided Student's T-test; asterisks indicate significance $p < 0.05$. Created with BioRender.com, licence number GI244FLSLH. Source data are provided as a Source Data file.

$Olig2$ ablation has been shown to reflect the number of OPCs that revert to an astrocytic fate. When $Olig2$ is deleted constitutively in OPCs beginning at E16.5 there is almost complete conversion of these cells to astrocytes[6]. However, deletion of Olig2 at P2 or P18 results in a 50% and 25% conversion to astrocytes, respectively[7,82]. From these results, we predict that an earlier inactivation of $Atrx$ in OPCs might yield a greater conversion to the astrocyte lineage in vivo. Our in vitro system is designed for the mass production of OPCs and allows for more cell division than would normally be observed in vivo, especially considering that the proliferation capacity of OPCs declines with age[83]. Accordingly, $Atrx^{Sox10Cre}$ mixed glial cultures exhibit a more drastic increase in conversion to astrocytes over a period of 9DIV. Mechanistically, Olig2 has been reported to directly repress key astrocytic fate determinants, including NFIA and GFAP, both of which were inappropriately induced in ATRX-null OPCs. NFIA can convert primed chromatin to active chromatin during early stages of astrocyte differentiation[73], and has been shown to activate $Gfap$ gene expression[84]. Although inactivation of Olig2 in OPCs causes a fate switch to astrocytes, other studies have revealed a more complex role of Olig2 in glial progenitors and astrocytes depending on the targeted cells, timing and brain region. For example, Olig2 has been reported to be transiently expressed in immature astrocytes of postnatal subventricular zone and to be required for white matter astrocyte maturation (Marshall 2005, Cai 2007).

Overall, our study suggests that myelination deficits caused by ATRX deficiency stems from cell-intrinsic functions of ATRX in the oligodendrocyte lineage, in addition to systemic mechanisms. Our findings could have implications in the treatment of myelin deficits in patients with disruptive $ATRX$ mutations. In addition to the potential benefits of thyroid hormone treatment, adjusting glial cell-fate imbalances and overcoming intrinsic defects in oligodendroglial cell maturation and the ensuing developmental dysmyelination could be important therapeutic targets to improve white matter defects in ATR-X syndrome patients.

Methods
Animal husbandry and genotyping
All procedures involving animals were conducted in accordance with the regulations of the Animals for Research Act of the Province of Ontario and approved by the University of Western Ontario Animal Care and Use Committee (AUPs 2017-048, 2021-049 and 2021-062). Mice were housed at a temperature of 20–26 °C and humidity between 40–60%, were exposed to 12-h light/12-h dark cycles and fed water and regular chow ad libitum. All mice were purchased from The Jackson

Laboratory except for the $Atrx^{loxP}$ mice which were provided by D. Higgs and R. Gibbons. Mice were euthanized with CO_2 inhalation or decapitation for neonatal mice (<10 days of age). The $Atrx^{loxP}$ mice have been described previously[85] (MGI:3528480). Briefly, $loxP$ sites flanking exon 18 of the $Atrx$ gene allow for deletion of this exon, destabilization of the mRNA and absence of the full-length ATRX protein[85]. Mating $Atrx^{loxP}$ female mice to males expressing Cre recombinase under the control of the $Foxg1$ promoter (129(Cg)-$Foxg1^{tm1(cre)Skm}$/J, RRID:IMSR_JAX:004337)[86] yielded male progeny with ATRX deficiency in the forebrain and anterior pituitary ($Atrx^{loxP}$;FoxG1Cre RRID:MGI:3530074) called $Atrx^{FoxG1Cre}$ for simplicity. Mating $Atrx^{loxP}$ female mice to males expressing Cre recombinase under the control of the Nex gene promoter[53,87] (Neurod6$^{tm1(cre)Kan}$, MGI:2668659) produced male progeny with ATRX deficiency in forebrain glutamatergic neurons ($Atrx^{loxP}$;NexCre or $Atrx^{NexCre}$ for simplicity). Mating $Atrx^{loxP}$ female mice to males expressing Cre recombinase under the control of the inducible Sox10 promoter[54] (CBA;B6-Tg(Sox10-icre/ERT2)388Wdr, MGI:5634390, RRID:IMSR JAX:027651), produced male progeny with $Atrx$ deficiency in OPCs ($Atrx^{loxP}$;Sox10Cre or $Atrx^{Sox10Cre}$) upon tamoxifen treatment. Two Cre-sensitive reporter lines were bred into the $Atrx^{loxP}$ mice for nuclei sorting and lineage tracing. The Sun1GFP allele (B6;129-Gt(ROSA)26Sor$^{tm5(CAG-Sun1/sfGFP)Nat}$/J, MGI:5614796, RRID: IMSR_JAX:021039) encodes the Sun1GFP fusion protein (located in the nuclear membrane) upon Cre-mediated recombination[55] and the Tomato-Ai14 (Ai14) allele (B6.Cg-Gt(ROSA)26Sor$^{tm14(CAG-tdTomato)Hze}$/J, MGI:3809524, RRID:IMSR JAX:007914)[59] expresses the tdTomato protein with red fluorescence in the cytoplasm and nucleus upon Cre recombination. Ear punch genomic DNA was used for PCR genotyping of the $Atrx$ floxed or wildtype alleles using the primers 17 F, 18 R and neoR as described previously[85]. The $FoxG1Cre$, $NexCre$, $Sox10Cre$, $Tomato-Ai14$ and $Sun1GFP$ genotyping primers are listed in Supplementary Table 1. This study focuses on ATRX, which is X-linked. Female carriers display highly skewed X chromosome inactivation toward the mutant allele and are usually phenotypically normal. Additionally, $Atrx^{FoxG1Cre}$ males are unable to mate to produce $Atrx^{FoxG1Cre}$ females.

Microarray analysis
Total forebrain RNA (10 μg) was isolated from three pairs of littermate-matched $Atrx^{FoxG1Cre}$ and control P17 mice using the RNeasy Mini kit (Qiagen Cat# 74104). cRNA was generated and hybridized to an Affymetrix Mouse Genome 430 2.0 Array at the London Regional Genomics Center (London, Canada). Probe signal intensities were generated using GCOS1.4 (Affymetrix Inc., Santa Clara, CA) using default values for the Statistical Expression algorithm parameters and a Target Signal

of 150 for all probe sets and a Normalization Value of 1. Gene level data was generated using the RNA preprocessor in GeneSpring GX 7.3.1 (Agilent Technologies Inc., Palo Alto, CA). Data were then transformed (measurements less than 0.01 set to 0.01), normalized per chip to the 50th percentile, and per gene to control samples. Probe sets representing *Atrx* transcripts were removed (10 sets). The remaining probe sets were filtered by fold change ≥1.5 between control and *Atrx*[FoxG1Cre] samples, and by confidence level of $p < 0.05$. Significantly over-represented GO categories were determined using the Enrichr web platform[88–90].

Thyroxine and tamoxifen injections

Subcutaneous injection of L-thyroxine (0.1 mg/kg; Sigma Cat# T2376-100MG) was performed daily on control and *Atrx*[Foxg1Cre] mice from birth (P0) until P14 as done previously[45]. Tamoxifen (10 mg; Cat# T5648, Sigma) was dissolved in 100 μL 95% ethanol at 65 °C for 10 mins, followed by dilution in 900 μL corn oil (Cat# C8267, Sigma). Lactating mothers were injected intraperitoneally daily with 2 mg tamoxifen for two (glial culture experiments) or three consecutive days[56].

Western blot analysis

Protein was extracted from P14 or P20 mouse forebrain and homogenized in RIPA buffer (150 mM NaCl), 1% NP-40, 50 mM Tris pH 8.0, 0.5% deoxycholic acid, 0.1% SDS, 0.2 mM PMSF, 0.5 mM NaF, 0.1 mM Na_3VO_4, 1× protease inhibitor cocktail (Millipore Sigma Cat# 11873580001). Homogenized tissue was incubated on ice for 20 minutes and centrifuged for 20 minutes at 1×10^4 RPM. Supernatant protein was quantified using the Bradford assay (BioRad Cat# 500-0006). Protein (30 μg) was resolved on a 12% SDS-PAGE and transferred to a 0.45 μm nitrocellulose membrane (BioRad Cat# 1620115). The membranes were probed with anti-MAG, mouse monoclonal (1:3000, Abcam Cat# ab89780, RRID:AB_2042411), anti-MOG, rabbit polyclonal (1:3000, Abcam Cat# ab32760, RRID:AB_2145529), or anti-MBP, rat monoclonal (1:3000, Abcam Cat# ab7349, RRID:AB_305869) antibodies at 4 °C overnight. This was followed by incubation with the appropriate horseradish peroxidase–conjugated secondary antibody for 1 h at room temperature: mouse anti-HRP (1:3,000, Santa Cruz Cat# sc-516102, RRID:AB_2687626), rabbit anti-HRP (1:5000, Jackson ImmunoResearch Cat# 111-036-003, RRID:AB_2337942) or rat anti-HRP (1:3,000, Santa Cruz Cat# sc-2006, RRID:AB_1125219). The membrane was incubated in enhanced chemiluminescent solution (Thermo Fisher Cat# 34095) before exposure using film (Progene Cat# 39-20810) or Universal Hood III (BioRad Cat# 731BR00882) and analyzed with Image Lab (BioRad, Version 4.1, 2012).

Mixed glial primary culture

Cre recombination in control and *Atrx*[Sox10Cre] pups was induced by IP injection of 2 mg tamoxifen to lactating mothers for two consecutive days (P0-P1)[56]. At P3, mouse cortices were dissected into MEM and tissue dissociated by pipetting with a P1000. Samples were then incubated at 37 °C with OPC papain solution (Worthington Cat# LS003124) for 20 min with constant inversion to prevent tissue aggregation. Papain was deactivated with serum-supplemented media for 10 min at room temperature followed by trituration with a flame polished Pasteur pipette. Samples were centrifuged at 300 g for 5 minutes and pellets resuspended in 1 mL DMEM supplemented with 10% FBS (Gibco Cat # 12483020), 1% Antibiotic-Antimycotic (Gibco Cat # 15240062) and 1% GlutaMax (Gibco Cat # 35050061). The cell suspension from each tube was added to a pre-equilibrated poly-L-lysine (1 mg/mL) coated 6 well plate in 1 mL of media or flasks with 5 mL of media. Cultures were incubated in the presence of 8.5% CO_2 in a tissue culture incubator for 3 h to allow cells to attach to the poly-L-lysine

substrate followed by a full media change. A 2/3 volume media change was performed every three days[60,61].

Immunofluorescence

P14 or P20 mice were trans-cardially perfused with PBS followed by 4% paraformaldehyde. Brains were fixed in 4% paraformaldehyde overnight. The next day, brains were washed 3 times for 5 min in PBS, sunk in 30% sucrose, flash-frozen on dry ice in Cryomatrix cryoprotectant (ThermoFisher Cat# 6769006), sectioned coronally at 8 μm thickness (Leica CM 3050 S) on Superfrost slides (Thermo Fisher Cat# 22-037-246) and stored at −80 °C with a desiccant (VWR, 61161-319). For immunofluorescence staining, slides were rehydrated in 1x PBS for 5 minutes, washed with PBS + 0.1% TritonX-100 (Millipore Sigma Cat# T8787), blocked with 10% normal goat serum diluted in washing solution (Millipore Sigma Cat# G9023) for 1 h and incubated with primary antibody overnight at 4 °C. Slides were washed 3 times for 5 min with PBS and incubated with secondary antibody for 1 h in the dark, and then washed twice for 5 min in PBS. Sections were counterstained with 1 μg/mL DAPI (Millipore Sigma Cat# D9542) for 5 min, washed for 5 min with PBS and mounted with Permafluor (Thermo Fisher Cat# TA-006-FM). Primary mixed glial cultures were fixed for immunofluorescence staining at 5, 6 and 9DIV (days in vitro) with 3% PFA at room temperature for 15 min. Cells were permeabilized with 0.1% TritonX-100/PBS (Millipore Sigma Cat# T8787), blocked with 10% normal goat serum in PBS (Millipore Sigma Cat# G9023) for 1 h and incubated with primary antibody overnight at 4 °C. The next day, flasks were washed 3 times for 5 min with PBS and incubated with the secondary antibody diluted in blocking solution for 1 h at room temperature. Cells were then counter-stained with 1 μg/mL DAPI (Millipore Sigma Cat# D9542) for 5 min, washed for 5 min with PBS and mounted with Permafluor (Thermo Fisher Cat# TA-006-FM). The following primary antibodies were used: anti-MOG, rabbit polyclonal (1:200, Abcam Cat# ab32760, RRID:AB_2145529), anti-MBP, rat monoclonal (1:50, Abcam Cat# ab7349, RRID:AB_305869), anti-ATRX, rabbit polyclonal (1:75, Santa Cruz Biotechnology Cat# sc-15408, RRID:AB_2061023), anti-Olig2, rabbit polyclonal (1:200, Millipore Cat# AB9610, RRID:AB_570666), anti-Olig2, mouse monoclonal (1:100, Sigma Cat# MABN50, RRID:AB_10807410) anti-S100β, rabbit polyclonal (1:200, Agilent Cat# Z0311, RRID:AB_10013383), anti-GFAP, rabbit polyclonal (1:200, Agilent Cat# Z0334, RRID:AB_10013382), anti-NG2, rabbit polyclonal (1:200, Millipore Cat# AB5320, RRID:AB_11213678), anti-PDGFRα, rabbit polyclonal (1:200 Abcam Cat# ab65258, RRID:AB_1141669), anti-APC, mouse monoclonal (Abcam Cat# ab16794, RRID:AB_443473), anti-Ki67, rabbit polyclonal (1:150 Abcam Cat# ab15580, RRID:AB_443209), anti-NFIA (1:100 Sigma-Aldrich Cat# HPA006111, RRID:AB_1854422) and anti-Sox10, rabbit polyclonal (1:100, Abcam Cat# ab155279, RRID:AB_2650603). The secondary antibodies used were goat anti-rabbit-Alexa Fluor 594 (1:800, Thermo Fisher Scientific, A-11012, RRID:AB_2534079), goat anti-rabbit-Alexa Fluor 488 (1:800, Thermo Fisher Scientific Cat# A-11008, RRID:AB_143165), goat anti-mouse-Alexa Fluor 594 (1:800 Thermo Fisher Scientific Cat# A-21125, RRID:AB_2535767), goat anti-mouse-Alexa Fluor 488 (1:800, Thermo Fisher Scientific Cat# A-11001, RRID:AB_2534069), goat anti-rat-Alexa Fluor 488 (1:800, Thermo Fisher Scientific, A-11006, RRID:AB_2534074) and goat anti-mouse-Alexa 647 (1:800, Thermo Fisher Scientific Cat# A-21235 RRID:AB 2535804). In Situ Cell Death Detection kit (Roche Cat# 11684795910) was used to assess cell death.

Fluorescence microscopy, imaging and cell counts

Immunofluorescence images were captured using an inverted microscope (DMI 6000b, Leica) outfitted with a digital camera (ORCA-ER, Hamamatsu). Openlab software (PerkinElmer Version 5.0, RRID:SCR_012158) was used for image capture. Image processing was

performed using Volocity (PerkinElmer Demo Version 6.0.1, RRID:SCR_002668) and Adobe Photoshop. Cell counts of brain sections and cultured cells were done in a blinded and randomized manner in control or experimental samples using Volocity (PerkinElmer Demo Version 6.0.1, RRID:SCR_002668). For brain sections, counts were performed in 2–10 sections per biological replicate and 3–4 biological replicates were counted for each genotype.

Fluorescence activated sorting of OPC nuclei

Fluorescence-activated nuclei sorting (FANS) was used to purify Sun1-GFP+ OPC nuclei from brain tissue[55,91]. Control or $Atrx^{Sox10Cre}$ forebrain tissue was homogenized in 500 µL homogenization buffer 20 mM Tricine KOH, 25 mM $MgCl_2$, 250 mM sucrose, 1 mM DTT, 0.15 mM spermine, 0.5 mM spermidine, 0.1% IGEPAL-630, 1× protease inhibitor cocktail (Millipore Sigma Cat# 11873580001), 1 µL/mL RNase inhibitor (Thermo Fisher Scientific Cat# 10777019). Samples were diluted to 7.5 mL with homogenization buffer and filtered through a 40 µm strainer. Filtered samples were layered on top of 7.5 mL cushion buffer consisting of 0.5 mM $MgCl_2$, 0.88 M sucrose, 0.5 mM DTT, 1× protease Inhibitor cocktail (Millipore Sigma Cat# 11873580001), 1 µL/mL RNase inhibitor (Thermo Fisher Scientific Cat# 10777019) and centrifuged at 2800 g for 20 mins at 4 °C. Nuclei were collected as a pellet, incubated for 10 min in 500 µL 4% FBS, 0.15 mM spermine, 0.5 mM spermidine, 1× protease inhibitor cocktail (Millipore Sigma Cat# 11873580001) and 1 µL/mL RNase inhibitor (Thermo Fisher Scientific Cat# 10777019) in PBS and resuspended by gentle pipetting. Nuclei were sorted using a Sony SH800 Cell Sorter and Sun1GFP+ nuclei were collected. Total RNA was immediately isolated from GFP+ nuclei with a single cell RNA purification kit (NorgenBiotek Cat# 51800).

Quantitative reverse transcriptase-PCR (qRT-PCR)

cDNA was prepared using 100 ng RNA from forebrain (P14 $Atrx^{FoxG1Cre}$), FANS-purified GFP+ OPC nuclei or from optic tracts (P20 $Atrx^{Sox10Cre}$) (RNeasy Mini kit; Qiagen Cat# 74104) and 1.5 µL of 100 ng/L of random hexamers (Integrated DNA Technologies Cat# 51-01-18-26) were diluted to a final volume of 12 µL with RNAse free water. Samples were heated at 65 °C for 10 min followed by addition of 4 µL first strand buffer (Thermo Fisher Scientific Cat# 18064014), 2 µL 100 mM DTT (Thermo Fisher Scientific Cat# 18064014), 0.8 µL 25 mM dNTPs, 0.5 µL RNaseOut (Thermo Fisher Scientific Cat# 10777019), 0.5 µL SuperScript II Reverse Transcriptase (Thermo Fisher Scientific Cat# 18064014) and 0.5 µL RNAse free water per sample. Samples were then incubated at 30 °C for 10 minutes and 42 °C for 45 min and stored at −20 °C. cDNA was amplified with iQ SYBR Green Master Mix (BioRad Cat# 1708884) using the standard curve Ct method of quantification. Experiments were performed on a Chromo-4 thermocycler (MJ Research/BioRad) and analyzed with Opticon Monitor 3 and GeneX (BioRad) software. Technical duplicates were completed for each sample. Conditions for amplification were as follows: 40 cycles of 95 °C for 10 s, 55–60 °C for 20 s, 72 °C for 30 s, and a final melting curve generated in increments of 0.5 °C per plate read. Primer sequences are listed in Supplementary Table 1.

RNA-seq analysis

RNA-seq libraries were prepared with 90 ng of RNA using VAHTSTM Total RNA-seq (H/M/R) Library Prep Kit for Illumina (Vazyme NR603-01) following the manufacturer's instructions. Libraries were sequenced at Canada's Michael Smith Genome Sciences Centre (BC Cancer Research, Vancouver, BC, Canada) using the Illumina HiseqX (Illumina Inc., San Diego, CA). On average, 50 million paired-end reads (150 bp) were obtained for each library. Raw reads were pre-processed with Trimgalore version 0.5.0, a wrapper tool around the sequence grooming tool cutadapt[92] with the following quality trimming and filtering parameters ('−phred33 −length 36 -q 5 −stringency 1 -e 0.1'). Each set of paired-end

reads was mapped against the *Mus musculus* GRCm38.p6 primary assembly downloaded from Ensembl[93] release 94 (https://useast.ensembl.org/Mus_musculus/Info/Annotation) using HISAT2 version 2.0.4[94]. SAMtools was then used to sort and convert SAM files. The read alignments and *Mus musculus* GRCm38 genome annotation were provided as input into StringTie v1.3.3[95] which returned gene and transcript abundances for each sample. We imported coverage and abundances for transcripts into R using the tximport[96] R/Bioconductor package and conducted differential analysis of transcript count data using the DESeq2 R/Bioconductor package[97]. We used the independent hypothesis weighting (IHW) method[98] to weight P values and adjust for multiple testing using the procedure of Benjamini Hochberg (BH)[99], transcripts p-values were then aggregated using the Lancaster method[100]. To generate the heatmap, gene level counts from the Stringtie results were transformed using variance stabilizing transformation (VST) method in DESeq2[97]. Z scores were then plotted using the pheatmap R package. Gene Ontology analysis was performed using Protein Analysis Through Evolutionary Relationships (Panther), http://www.pantherdb.org[101]. Gene cluster analysis was performed using TOPPCluster[102].

Chromatin immunoprecipitation (ChIP)

For ATRX ChIP, cortices from fifteen P0.5 pups were dissected and OPCs were cultured for 9 DIV in a mixed glial culture. OPCs were then physically separated from other cells by shaking at 220 rpm overnight in a tissue culture incubator at 5% CO_2[60,61]. OPCs were pooled, homogenized and passed through a 70 µm strainer (Fisher Cat#22363548). For H3K27Ac ChIP, 3 to 4 optic tracts were dissected from either control or $Atrx^{Sox10Cre}$ P20 mice. Tissue was minced and triturated in DMEM and filtered through a 70 µm strainer (Fisher Cat#22363548).

OPCs were first crosslinked with 0.002 M ethylene glycol bis (succinimidyl succinate) (EGS, Thermo Fisher Scientific Cat # 21565) at room temperature for 45 min with constant mixing[103]. Both OPC and optic tract samples were crosslinked with 1% formaldehyde at room temperature for 20 min (OPCs) or 10 min (optic tracts) with constant mixing. Samples were quenched in 0.125 M glycine for 2 min at room temperature and centrifuged at 700 g for 5 min. Pellets were washed twice with 10 mL cold PBS and stored at −80 °C.

Chromatin was sonicated in a Bioruptor Pico Sonication Device (Diagenode Cat# B01060010) for 6 cycles (OPCs) or 13 cycles (optic tracts). For OPCs, protein G Dynabeads (50 µL, Invitrogen Cat# 10009D) were loaded with either 10 µg anti-ATRX rabbit polyclonal antibody (Abcam Cat# ab97508, RRID:AB_10680289) or anti-IgG rabbit polyclonal antibody (Thermo Fisher Scientific Cat# 02-6102, RRID:AB_2532938) for 4 h with rotation at 4 °C. For optic tracts, protein G Dynabeads (20 µL, Invitrogen Cat# 10009D) were loaded with either 2.5 µg anti-H3K27Ac rabbit polyclonal antibody (Abcam Cat# ab4729, RRID:AB_2118291) or anti-IgG rabbit polyclonal antibody (Thermo Fisher Scientific Cat# 02-6102, RRID:AB_2532938) for 1 h with rotation at 4 °C.

Chromatin lysates (50 µg per IP for OPCs, 20ug per IP for optic tracts) were precleared with 100 uL (OPCs) or 20ul (optic tracts) protein G Dynabeads (Invitrogen Cat# 10009D) for 1 h at 4 °C. Precleared lysate and antibody-bound beads were combined and incubated at 4 °C overnight with rotation. The next day, beads were washed five times and eluted for 15 min at room temperature followed by a second elution for 20 minutes at 65 °C[103]. Crosslinking was reversed by adding 5 M NaCl at 65 °C for 4 h. Samples were treated with 1 µL 10 mg/mL RNase A at 37 °C for 30 min then 1 µL 20 µg/mL proteinase K for 1 h at 45 °C. 1/10th of precleared chromatin lysate was treated the same and used as input.

ChIP-seq analysis

ChIP-seq libraries were made with Accel-NGS 1S Plus DNA library preparation kit (Swift Biosciences) following the manufacturer's

instructions. Libraries were sequenced with Illumina NovaSeq 6000 and ~25 million paired-end reads (150 bp) were obtained from each library. The paired-end reads in Fastq format were trimmed with Trim Galore (v.0.6.6), a wrapper tool around Cutadapt[92] package, and were then aligned to the mouse genome (mm10) using Bowtie2(v.2.4.4) with the default parameters[104]. SAMtools (v.1.12) was then used to create and sort BAM files from the aligned reads recorded in SAM format[105]. The duplicated reads were marked with MarkDuplicates function from Picard (v.2.26.3). The mitochondrial DNA reads and blacklist regions of the genome were filtered out using Bedtools intersect (v.2.30.0). MACS2 (v.2.2.7.1)[62] broadPeak mode was used to call the peaks from the filtered BAM files with input control. R package csaw (v.1.26.0)[106] was used to count the reads in 300 bp non-overlapping windows. Background noise was estimated by counting reads in 2000bp bins. We selected 300 bp windows that have a signal higher than log2(3) above background. Windows were then merged if less than 100 bp apart but did not extend above 5 kb width. Rtracklayer (v.1.52.1)[107] package was then used to export the filtered windows in a BED format. FindMotifsGenome.pl and annotatePeaks.pl functions from HOMER (v.4.10)[108] were used to find enriched DNA motifs in the peak lists and annotate the peaks in the genome, respectively. The ATRX ChIP Bigwig track was generated using Deeptools2 bamCompare (v.3.5.2)[109] with the parameter "−scaleFactorsMethod SES" (input control was used for normalization). plotHeatmap and plotProfile functions of Deeptools2 were also used to compare ATRX enrichment at peaks of publicly available ChIP-seq datasets. H3K27Ac and Olig2 ChIP data was downloaded from NCBI Gene Expression Omnibus (GSE42454). UCSC liftOver tool was used to convert peak coordinates from rn4 to mm10 genome assembly. The raw fastq files of HDAC3 and p300 in OPCs were downloaded from NCBI GSE76412. The reads were aligned to rn4 genome assembly using Bowtie2 (v.2.4.4). SAMtools (v.1.12) was then used to generate and filter BAM files. Peaks were called as described for ATRX ChIP. UCSC liftOver was then used to convert peak coordinates from rn4 to mm10 genome assembly. Chd7 and Chd8 ChIP peaks in OPCs were downloaded from NCBI GSE116601. Brn1, Oct6, and Sox2 ChIP-seq data from mouse neural stem cell line NS5 was downloaded (in wig format) from NCBI GSE69859. Wig files were converted to bigwig files using wigToBigWig from rtracklayer (v.1.52.1). Bigwig files were then converted to bedGraph files using UCSC bigWigToBedGraph tool. UCSC liftOver was then used to convert peak coordinates from mm8 to mm10 genome assembly.

Statistical analysis
Statistical analysis was performed using GraphPad Prism6 software (6.05; GraphPad Software Inc.) and results are expressed as the mean +/− SEM or SD. Two independent data sets were compared with the Student's T-test (unpaired, two-sided). Multiple independent data sets were compared with a one-way ANOVA with post-hoc Tukey's HSD. P values of 0.05 or less were considered to indicate significance.

Reporting summary
Further information on research design is available in the Nature Portfolio Reporting Summary linked to this article.

Data availability
The datasets for the $Atrx^{Foxg1Cre}$ RNA microarrays have been deposited in the National Centre for Biotechnology Information Gene Expression Omnibus Database under accession code GSE210863, ATRX OPC nuclei RNA-seq and ATRX OPC ChIP-seq data can be accessed at NCBI Bioproject PRJNA866270. Other datasets used in this study can be accessed at the NCBI GEO Database under the accession codes GSE116601 (ChIP-seq OPC CHD7 and CHD8), GSE42454 (ChIP-seq OPC Olig2 and H3K27Ac), GSE76412 (ChIP-seq OPC HDAC3 and P300) and GSE69859 (ChIP-seq NSC, Sox2, Brn-1 and Oct6). Source data are provided with this paper.

References
1. Nave, K. A. & Werner, H. B. Myelination of the nervous system: mechanisms and functions. *Ann. Rev. Cell Dev. Biol.* **30**, 503–533 (2014).
2. Sauvageot, C. M. & Stiles, C. D. Molecular mechanisms controlling cortical gliogenesis. *Curr. Opin. Neurobiol.* **12**, 244–249 (2002).
3. Zhou, Q. & Anderson, D. J. The bHLH transcription factors OLIG2 and OLIG1 couple neuronal and glial subtype specification. *Cell* **109**, 61–73 (2002).
4. Zhou, Q., Choi, G. & Anderson, D. J. The bHLH transcription factor Olig2 promotes oligodendrocyte differentiation in collaboration with Nkx2.2. *Neuron* **31**, 791–807 (2001).
5. Cai, J. et al. A crucial role for Olig2 in white matter astrocyte development. *Development* **134**, 1887 (2007).
6. Zhu, X. et al. Olig2-dependent developmental fate switch of NG2 cells. *Development* **139**, 2299–2307 (2012).
7. Zuo, H., Wood, W. M., Sherafat, A. & Hill, R. A. *Age-Dependent Decline in Fate Switch from NG2 Cells to Astrocytes After Olig2 Deletion*. **38**, 2359–2371, (2018).
8. Finzsch, M., Stolt, C. C., Lommes, P. & Wegner, M. Sox9 and Sox10 influence survival and migration of oligodendrocyte precursors in the spinal cord by regulating PDGF receptor alpha expression. *Development* **135**, 637–646 (2008).
9. Kuspert, M., Hammer, A., Bosl, M. R. & Wegner, M. Olig2 regulates Sox10 expression in oligodendrocyte precursors through an evolutionary conserved distal enhancer. *Nucleic Acids Res.* **39**, 1280–1293 (2011).
10. Yu, Y. et al. Olig2 targets chromatin remodelers to enhancers to initiate oligodendrocyte differentiation. *Cell* **152**, 248–261 (2013).
11. Nishiyama, A., Lin, X. H., Giese, N., Heldin, C. H. & Stallcup, W. B. Interaction between NG2 proteoglycan and PDGF alpha-receptor on O2A progenitor cells is required for optimal response to PDGF. *J. Neurosci. Res.* **43**, 315–330 (1996).
12. Nishiyama, A., Lin, X. H., Giese, N., Heldin, C. H. & Stallcup, W. B. Co-localization of NG2 proteoglycan and PDGF alpha-receptor on O2A progenitor cells in the developing rat brain. *J. Neurosci. Res.* **43**, 299–314 (1996).
13. Pringle, N. P., Mudhar, H. S., Collarini, E. J. & Richardson, W. D. PDGF receptors in the rat CNS: during late neurogenesis, PDGF alpha-receptor expression appears to be restricted to glial cells of the oligodendrocyte lineage. *Development* **115**, 535–551 (1992).
14. Makagiansar, I. T., Williams, S., Mustelin, T. & Stallcup, W. B. Differential phosphorylation of NG2 proteoglycan by ERK and PKCalpha helps balance cell proliferation and migration. *J. Cell Biol.* **178**, 155–165 (2007).
15. Noble, M., Murray, K., Stroobant, P., Waterfield, M. D. & Riddle, P. Platelet-derived growth factor promotes division and motility and inhibits premature differentiation of the oligodendrocyte/type-2 astrocyte progenitor cell. *Nature* **333**, 560–562 (1988).
16. Pringle, N. et al. PDGF A chain homodimers drive proliferation of bipotential (O-2A) glial progenitor cells in the developing rat optic nerve. *EMBO J.* **8**, 1049–1056 (1989).
17. Emery, B. et al. Myelin gene regulatory factor is a critical transcriptional regulator required for CNS myelination. *Cell* **138**, 172–185 (2009).
18. Mitew, S. et al. Mechanisms regulating the development of oligodendrocytes and central nervous system myelin. *Neuroscience* **276**, 29–47 (2014).
19. Li, H., Lu, Y., Smith, H. K. & Richardson, W. D. Olig1 and Sox10 interact synergistically to drive myelin basic protein transcription in oligodendrocytes. *J. Neurosci.: Off. J. Soc. Neurosci.* **27**, 14375–14382 (2007).
20. Stolt, C. C. et al. Terminal differentiation of myelin-forming oligodendrocytes depends on the transcription factor Sox10. *Genes Dev.* **16**, 165–170 (2002).

21. Wei, Q., Miskimins, W. K. & Miskimins, R. Sox10 acts as a tissue-specific transcription factor enhancing activation of the myelin basic protein gene promoter by p27Kip1 and Sp1. *J. Neurosci. Res.* **78**, 796–802 (2004).

22. Qi, Y. et al. Control of oligodendrocyte differentiation by the Nkx2.2 homeodomain transcription factor. *Development* **128**, 2723–2733 (2001).

23. Farsetti, A., Mitsuhashi, T., Desvergne, B., Robbins, J. & Nikodem, V. M. Molecular basis of thyroid hormone regulation of myelin basic protein gene expression in rodent brain. *J. Biolog. Chem.* **266**, 23226–23232 (1991).

24. Ibarrola, N. & Rodríguez-Peña, A. Hypothyroidism coordinately and transiently affects myelin protein gene expression in most rat brain regions during postnatal development. *Brain Res.* **752**, 285–293 (1997).

25. Dong, H. et al. Identification of thyroid hormone receptor binding sites and target genes using ChIP-on-Chip in developing mouse cerebellum. *PLoS One* **4**, e4610 (2009).

26. Franklin, R. J. M. & ffrench-Constant, C. Remyelination in the CNS: from biology to therapy. *Nat. Rev. Neurosci.* **9**, 839 (2008).

27. Courchesne, E., Press, G. A. & Yeung-Courchesne, R. Parietal lobe abnormalities detected with MR in patients with infantile autism. *AJR. Am. J. Roentgenol.* **160**, 387–393 (1993).

28. Wolkin, A. et al. Structural magnetic resonance image averaging in schizophrenia. *Am. J. Psychiatr.* **155**, 1064–1073 (1998).

29. Iwase, S. et al. Epigenetic etiology of intellectual disability. *J. Neurosci.* **37**, 10773 (2017).

30. Gibbons, R. J., Picketts, D. J., Villard, L. & Higgs, D. R. Mutations in a putative global transcriptional regulator cause X-linked mental retardation with alpha-thalassemia (ATR-X syndrome). *Cell* **80**, 837–845 (1995).

31. Gibbons, R. J. & Higgs, D. R. Molecular-clinical spectrum of the ATR-X syndrome. *Am. J. Med. Genet.* **97**, 204–212 (2000).

32. Gibbons, R. J., Picketts, D. J. & Higgs, D. R. Syndromal mental retardation due to mutations in a regulator of gene expression. *Hum. Mol. Genet.* **4**, 1705–1709 (1995).

33. Wada, T. et al. Neuroradiologic features in X-linked α-Thalassemia/mental retardation syndrome. *American Journal of Neuroradiology* **34**, 2034–2038 (2013).

34. Lee, J. S. et al. Alpha-thalassemia X-linked intellectual disability syndrome identified by whole exome sequencing in two boys with white matter changes and developmental retardation. *Gene* **569**, 318–322 (2015).

35. Giacomini, T. et al. Epileptic encephalopathy, myoclonus-dystonia, and premature pubarche in siblings with a novel C-terminal truncating mutation in ATRX gene. *Neuropediatrics* **50**, 327–331 (2019).

36. Picketts, D. J. et al. ATRX encodes a novel member of the SNF2 family of proteins: mutations point to a common mechanism underlying the ATR-X syndrome. *Hum. Mol. Genet.* **5**, 1899–1907 (1996).

37. Kernohan, K. D. et al. ATRX partners with cohesin and MeCP2 and contributes to developmental silencing of imprinted genes in the brain. *Dev. Cell* **18**, 191–202 (2010).

38. Kernohan, K. D., Vernimmen, D., Gloor, G. B. & Berube, N. G. Analysis of neonatal brain lacking ATRX or MeCP2 reveals changes in nucleosome density, CTCF binding and chromatin looping. *Nucleic Acids Res.* **42**, 8356–8368 (2014).

39. Sarma, K. et al. ATRX directs binding of PRC2 to Xist RNA and Polycomb targets. *Cell* **159**, 869–883 (2014).

40. Levy, M. A., Fernandes, A. D., Tremblay, D. C., Seah, C. & Bérubé, N. G. The SWI/SNF protein ATRX co-regulates pseudoautosomal genes that have translocated to autosomes in the mouse genome. *BMC Genomics* **9**, 468 (2008).

41. Levy, M. A., Kernohan, K. D., Jiang, Y. & Bérubé, N. G. ATRX promotes gene expression by facilitating transcriptional elongation through guanine-rich coding regions. *Hum. Mol. Genet.* **24**, 1824–1835 (2015).

42. Bagheri-Fam, S., Alankarage, D., Frost, E. R. & Harley, V. R. Dataset of differentially expressed genes in mouse P12 testes in response to the loss of ATRX in Sertoli cells. *Data Brief* **42**, 108230 (2022).

43. Bagheri-Fam, S. et al. Defective survival of proliferating Sertoli cells and androgen receptor function in a mouse model of the ATR-X syndrome. *Hum. Mol. Genet.* **20**, 2213–2224 (2011).

44. Ratnakumar, K. et al. ATRX-mediated chromatin association of histone variant macroH2A1 regulates α-globin expression. *Genes Dev.* **26**, 433–438 (2012).

45. Rowland, M. E., Jiang, Y., Beier, F. & Bérubé, N. G. Inactivation of hepatic ATRX in Atrx Foxg1cre mice prevents reversal of aging-like phenotypes by thyroxine. *Aging (Albany NY)* **10**, 1223–1238 (2018).

46. Watson, L. A. et al. Atrx deficiency induces telomere dysfunction, endocrine defects, and reduced life span. *J. Clin. Invest.* **123**, 2049–2063 (2013).

47. Franco, P. G., Silvestroff, L., Soto, E. F. & Pasquini, J. M. Thyroid hormones promote differentiation of oligodendrocyte progenitor cells and improve remyelination after cuprizone-induced demyelination. *Exp. Neurol.* **212**, 458–467 (2008).

48. Almazan, G., Honegger, P. & Matthieu, J. M. Triiodothyronine stimulation of oligodendroglial differentiation and myelination. A developmental study. *Dev. Neurosci.* **7**, 45–54 (1985).

49. Barres, B. A., Lazar, M. A. & Raff, M. C. A novel role for thyroid hormone, glucocorticoids and retinoic acid in timing oligodendrocyte development. *Development* **120**, 1097–1108, https://doi.org/10.1242/dev.120.5.1097 (1994).

50. Fernandez, M., Pirondi, S., Manservigi, M., Giardino, L. & Calza, L. Thyroid hormone participates in the regulation of neural stem cells and oligodendrocyte precursor cells in the central nervous system of adult rat. *Euro. J. Neurosci.* **20**, 2059–2070 (2004).

51. Noguchi, T., Sugisaki, T., Satoh, I. & Kudo, M. Partial restoration of cerebral myelination of the congenitally hypothyroid mouse by parenteral or breast milk administration of thyroxine. *J. Neurochem.* **45**, 1419–1426 (1985).

52. Tosic, M. et al. Triiodothyronine has diverse and multiple stimulating effects on expression of the major myelin protein genes. *J. Neurochem.* **59**, 1770–1777 (1992).

53. Goebbels, S. et al. Genetic targeting of principal neurons in neocortex and hippocampus of NEX-Cre mice. *Genesis (New York, N.Y.: 2000)* **44**, 611–621 (2006).

54. McKenzie, I. A. et al. Motor skill learning requires active central myelination. *Science (New York, N.Y.)* **346**, 318–322 (2014).

55. Mo, A. et al. Epigenomic signatures of neuronal diversity in the mammalian brain. *Neuron* **86**, 1369–1384 (2015).

56. Harris, M. L. et al. A dual role for SOX10 in the maintenance of the postnatal melanocyte lineage and the differentiation of melanocyte stem cell progenitors. *PLoS Genet.* **9**, e1003644 (2013).

57. Takebayashi, H. et al. The basic helix-loop-helix factor olig2 is essential for the development of motoneuron and oligodendrocyte lineages. *Curr. Biol.: CB* **12**, 1157–1163 (2002).

58. Lu, Q. R. et al. Common developmental requirement for Olig function indicates a motor neuron/oligodendrocyte connection. *Cell* **109**, 75–86 (2002).

59. Madisen, L. et al. A robust and high-throughput Cre reporting and characterization system for the whole mouse brain. *Nat. Neurosci.* **13**, 133–140 (2010).

60. Chen, Y. et al. Isolation and culture of rat and mouse oligodendrocyte precursor cells. *Nat. Protocols* **2**, 1044–1051 (2007).

61. O'Meara, R. W., Ryan, S. D., Colognato, H. & Kothary, R. Derivation of enriched oligodendrocyte cultures and oligodendrocyte/

neuron myelinating co-cultures from post-natal murine tissues. *J. Visual. Exp.: JoVE*, https://doi.org/10.3791/3324 (2011).

62. Zhang, Y. et al. Model-based analysis of ChIP-Seq (MACS). *Genome Biol*. **9**, R137 (2008).

63. Mistri, T. K. et al. Selective influence of Sox2 on transcription factor binding in embryonic and neural stem cells. *EMBO Rep*. **16**, 1177–1191 (2015).

64. Zhang, L. et al. Hdac3 interaction with p300 histone acetyltransferase regulates the oligodendrocyte and astrocyte lineage fate switch. *Dev. Cell* **36**, 316–330 (2016).

65. He, D. et al. Chd7 cooperates with Sox10 and regulates the onset of CNS myelination and remyelination. *Nat. Neurosci*. **19**, 678–689 (2016).

66. Marie, C. et al. Oligodendrocyte precursor survival and differentiation requires chromatin remodeling by Chd7 and Chd8. *Proc. Natl Acad. Sci*. **115**, E8246–E8255 (2018).

67. Zhao, C. et al. Dual requirement of CHD8 for chromatin landscape establishment and histone methyltransferase recruitment to promote CNS myelination and repair. *Dev. Cell* **45**, 753–768.e758 (2018).

68. Yue, T. A critical role for dorsal progenitors in cortical myelination. *J. Neurosci*. **26**, 1275–1280 (2006).

69. Creyghton, M. P. et al. Histone H3K27ac separates active from poised enhancers and predicts developmental state. *Proc. Natl. Acad. Sci*. **107**, 21931–21936 (2010).

70. Cahoy, J. D. et al. A Transcriptome database for astrocytes, neurons, and oligodendrocytes: a new resource for understanding brain development and function. *J. Neurosci*. **28**, 264–278.

71. Weng, Q. et al. Single-cell transcriptomics uncovers glial progenitor diversity and cell fate determinants during development and gliomagenesis. *Cell Stem Cell* **24**, 707–723 e708 (2019).

72. Hachem, S. et al. Spatial and temporal expression of S100B in cells of oligodendrocyte lineage. *Glia* **51**, 81–97 (2005).

73. Tiwari, N. et al. Stage-specific transcription factors drive astrogliogenesis by remodeling gene regulatory landscapes. *Cell Stem Cell* **23**, 557–571.e558 (2018).

74. Kang, P. et al. Sox9 and NFIA coordinate a transcriptional regulatory cascade during the initiation of gliogenesis. *Neuron* **74**, 79–94 (2012).

75. Parras, C., Marie, C., Zhao, C. & Lu, Q. R. Chromatin remodelers in oligodendroglia. *Glia* **68**, 1604–1618 (2020).

76. Gibson, E. M. et al. Neuronal activity promotes oligodendrogenesis and adaptive myelination in the mammalian brain. *Science (New York, N.Y.)* **344**, 1252304 (2014).

77. Barres, B. A. & Raff, M. C. Proliferation of oligodendrocyte precursor cells depends on electrical activity in axons. *Nature* **361**, 258–260 (1993).

78. Gautier, H. O. B. et al. Neuronal activity regulates remyelination via glutamate signalling to oligodendrocyte progenitors. *Nat. Commun*. **6**, 8518–8518 (2015).

79. Bernier, R. et al. Disruptive CHD8 mutations define a subtype of autism early in development. *Cell* **158**, 263–276 (2014).

80. Cotney, J. et al. The autism-associated chromatin modifier CHD8 regulates other autism risk genes during human neurodevelopment. *Nat. Commun*. **6**, 6404 (2015).

81. Stolerman, E. S. et al. Genetic variants in the KDM6B gene are associated with neurodevelopmental delays and dysmorphic features. *Am. J. Med. Genet. Part A* **179**, 1276–1286 (2019).

82. Zhu, X., Bergles, D. E. & Nishiyama, A. NG2 cells generate both oligodendrocytes and gray matter astrocytes. *Development* **135**, 145–157 (2008).

83. Young, K. M. et al. Oligodendrocyte dynamics in the healthy adult CNS: evidence for myelin remodeling. *Neuron* **77**, 873–885 (2013).

84. Cebolla, B. & Vallejo, M. Nuclear factor-I regulates glial fibrillary acidic protein gene expression in astrocytes differentiated from cortical precursor cells. *J. Neurochem*. **97**, 1057–1070.

85. Berube, N. G. et al. The chromatin-remodeling protein ATRX is critical for neuronal survival during corticogenesis. *J. Clin. Invest*. **115**, 258–267 (2005).

86. Hebert, J. M. & McConnell, S. K. Targeting of cre to the Foxg1 (BF-1) locus mediates loxP recombination in the telencephalon and other developing head structures. *Developmental biology* **222**, 296–306 (2000).

87. Schwab, M. H. et al. Neuronal basic helix-loop-helix proteins (NEX and BETA2/Neuro D) regulate terminal granule cell differentiation in the hippocampus. *J. Neurosci.: Off. J. Soc. Neurosci*. **20**, 3714–3724 (2000).

88. Chen, E. Y. et al. Enrichr: interactive and collaborative HTML5 gene list enrichment analysis tool. *BMC Bioinform*. **14**, 128 (2013).

89. Kuleshov, M. V. et al. Enrichr: a comprehensive gene set enrichment analysis web server 2016 update. *Nucleic Acids Res*. **44**, W90–W97 (2016).

90. Xie, Z. et al. Gene set knowledge discovery with enrichr. *Curr. Protoc*. **1**, e90 (2021).

91. Pena-Ortiz, M. A. et al. Selective isolation of mouse glial nuclei optimized for reliable downstream omics analyses. *J. Neurosci. Methods* **369**, 109480 (2022).

92. Martin, M. Cutadapt removes adapter sequences from high-throughput sequencing reads. *EMBnet. J*. **17**, 10 (2011).

93. Zerbino, D. R. et al. Ensembl 2018. *Nucleic acids research* **46**, D754–D761 (2018).

94. Kim, D., Langmead, B. & Salzberg, S. L. HISAT: a fast spliced aligner with low memory requirements. *Nat. Methods* **12**, 357–360.

95. Pertea, M. et al. StringTie enables improved reconstruction of a transcriptome from RNA-seq reads. *Nat. Biotechnol*. **33**, 290–295 (2015).

96. Soneson, C., Love, M. I. & Robinson, M. D. Differential analyses for RNA-seq: transcript-level estimates improve gene-level inferences. *F1000Res*. **4**, 1521 (2016).

97. Love, M. I., Huber, W. & Anders, S. Moderated estimation of fold change and dispersion for RNA-seq data with DESeq2. *Genome Biol*. **15**, 550 (2014).

98. Ignatiadis, N., Klaus, B., Zaugg, J. B. & Huber, W. Data-driven hypothesis weighting increases detection power in genome-scale multiple testing. *Nat. Methods* **13**, 577–580 (2016).

99. Benjamini, Y. & Hochberg, Y. Controlling the false discovery rate: a practical and powerful approach to multiple testing. *J. Royal Stat. Soc.: Series B (Methodological)* **57**, 289–300 (1995).

100. Yi, L., Pimentel, H., Bray, N. L. & Pachter, L. Gene-level differential analysis at transcript-level resolution. *Genome Biology* **19**, 53 (2018).

101. Mi, H. et al. PANTHER version 16: a revised family classification, tree-based classification tool, enhancer regions and extensive API. *Nucleic acids research* **49**, D394–D403.

102. Kaimal, V., Bardes, E. E., Tabar, S. C., Jegga, A. G. & Aronow, B. J. ToppCluster: a multiple gene list feature analyzer for comparative enrichment clustering and network-based dissection of biological systems. *Nucleic Acids Res*. **38**, W96–W102.

103. Truch, J., Telenius, J., Higgs, D. R. & Gibbons, R. J. How to tackle challenging ChIP-Seq, with long-range cross-linking, using ATRX as an example. *Methods Mol. Biol. (Clifton, N.J.)* **1832**, 105–130 (2018).

104. Langmead, B. & Salzberg, S. L. Fast gapped-read alignment with Bowtie 2. *Nat. Methods* **9**, 357–359 (2012).

105. Danecek, P. et al. Twelve years of SAMtools and BCFtools. *GigaScience* **10**, giab008 (2021).

106. Lun, A. T. L. & Smyth, G. K. csaw: a Bioconductor package for differential binding analysis of ChIP-seq data using sliding windows. *Nucleic Acids Res.* **44**, e45–e45 (2016).
107. Lawrence, M., Gentleman, R. & Carey, V. rtracklayer: an R package for interfacing with genome browsers. *Bioinformatics* **25**, 1841–1842 (2009).
108. Heinz, S. et al. Simple combinations of lineage-determining transcription factors prime cis-regulatory elements required for macrophage and B cell identities. *Mol. Cell* **38**, 576–589 (2010).
109. Ramírez, F. et al. deepTools2: a next generation web server for deep-sequencing data analysis. *Nucleic Acids Res.* **44**, W160–W165 (2016).

Author contributions

M.E.R. and N.G.B. designed the study. V.D. analyzed the RNA-seq data, assisted in the ChIPseq analyses and reviewed the manuscript. M.E.R., Y.J., S.S. and M.A.P.O. acquired the data. M.E.R., Y.J., A.G. and N.G.B. analyzed data and generated figures. M.E.R. and N.G.B. wrote the manuscript.

Competing interests

The authors declare no competing interests.

Additional information

Supplementary information The online version contains supplementary material available at https://doi.org/10.1038/s41467-023-42752-y.

Correspondence and requests for materials should be addressed to Nathalie G. Bérubé.

Peer review information *Nature Communications* thanks Q. Richard Lu, and the other, anonymous, reviewer(s) for their contribution to the peer review of this work.

Reprints and permissions information is available at http://www.nature.com/reprints

Publisher's note Springer Nature remains neutral with regard to jurisdictional claims in published maps and institutional affiliations.